Geophysical Journal International

Geophys. J. Int. (2018) **215,** 924–941
doi: 10.1093/gji/ggy308
Advance Access publication 2018 August 01
GJI Seismology

Random kinematics of unbounded earthquake rupture propagation simulated using a cellular model

A.A. Gusev[1,2]

[1] *Institute of Volcanology and Seismology, Far East Branch, Russian Academy of Sciences, Petropavlosk-Kamchatskii, Russia. E-mail:* gusev@emsd.ru
[2] *Geophysical Survey, Kamchatka Branch, Russian Academy of Sciences, Petropavlosk-Kamchatskii, Russia*

Accepted 2018 July 31. Received 2018 July 13; in original form 2018 January 06

SUMMARY

Spectra of high-frequency (HF) waves radiated by earthquake sources have specific features: above the common corner frequency f_{c1} they manifest second corner frequency, f_{c2}; and beyond, a plateau in acceleration spectrum. To explain these features, convoluted, 'lacy' geometry of earthquake rupture front was recently proposed. In order to realize such geometry, random space–time functions were used; this simple approach permitted to reproduce both the mentioned spectral properties. However, the random structure of the front was introduced in that earlier study in an *a priori* manner. Presently, stochastic evolution of a rupture is described in a less formal way, employing a continuous-time cellular model. Each cell of a model geological fault is occupied by an automaton, with three possible states: intact, failing, or broken. A failing cell can 'ignite', after certain delay time Δt, failures in neighbour cells. Local values of Δt are fixed in advance and represent a realization of self-similar random 2-D field. A local Δt value is believed to reflect local resistance to failure: the stronger a cell is, the larger is its Δt. Through a succession of local failures, a convoluted or even multiply connected rupture front is formed. Viewed at low resolution, such front occupies a certain strip of finite width. Numerically, this width can be described through the rms width parameter, w. As was shown in earlier simulations, there exists a close relationship between w and f_{c2}: $f_{c2}\propto 1/w$. Using this relationship one can verify a stochastic fault model through comparison of the predicted scaling behaviour of f_{c2} against the observed one. For the relationships of the kind $\log f_{ck} = -\beta_k \log M_0 + const$, observations give values of β_2 in the range 0.16–0.27, against $\beta_1 \approx 1/3$ for the common corner frequency, f_{c1}. Thus, the behavior of f_{c1} agrees with the similarity assumption, whereas that of f_{c2} does not. Through comparison of calculated estimates for β_2 and for rupture velocity with their observed values, realistic ranges of parameters of the developed model were obtained. With appropriate parameter ranges selected, the current model successively reproduces both the observed range of β_2 and the observed range of average earthquake rupture velocity, $(0.5–0.8)c_S$. When a simulated rupture front history is combined with a plausible 2-D field of local stress drop, broad-band time histories can be generated, with verisimilar spectra. These have two corner frequencies and a plateau in acceleration source spectrum. It was found that permissible variation of model parameters can significantly modify, at given M_0 and stress drop, the relative levels of HF radiation from a source; this may give better insight into causes of variability of strong motion amplitudes.

Key words: Numerical modelling; Earthquake dynamics; Earthquake source observations; Statistical seismology; Dynamics and mechanics of faulting.

1. INTRODUCTION

The property of incoherence of high-frequency (HF) radiation from an earthquake source has been noted by Kostrov (1975). Boore & Joyner (1978) and Israel & Nur (1979) saw the cause of incoherence in two random fields over the fault area: first, of random final slip, and, second, of random local/instant rupture velocity. Joyner (1991) noticed that within such a model, one should observe the specific variation of body wave pulse shapes and their spectra at different angular positions on focal sphere: pulses are compressed or expanded with preserved overall shape, and their spectra, accordingly, are expanded or compressed. At realistic rupture velocities, v_r, comparable to shear wave velocity, c_S, this would result in expressed angular dependence of acceleration amplitudes: 'forward' radiation, that is along rupture propagation direction, must be much more powerful than 'backward' radiation. Whereas such directivity does exist for velocity (or displacement) amplitudes, it is almost inconspicuous for acceleration amplitudes or macroseismic intensity. Thus, the initial idea—to associate incoherence directly with random slip or random local rupture velocity—did not work. Negligible directivity of HF strong motion amplitudes with respect to rupture direction was a standard view of engineering seismology prior to the beginning of 1990s, both for velocities and accelerations. After observation of expressed directivity of peak velocity in records of Landers 1992 earthquake, 'forward directivity' became a standard concept in modern engineering seismology (Somerville *et al*. 1997; and later work). However, with respect to peak accelerations no directivity corrections were found necessary. In spectral domain, clear dependence of directivity on the considered frequency range was discussed by Bernard & Herrero (1994).

The simplest way to explain radiation incoherence is to distribute over the fault surface many independent point subsources of dislocation kind or to cover this surface with random radiating patches; the key property is statistically independent random time histories of subsources (Hanks 1979; Gusev 1983; Koyama & Shimada 1985). For a particular frequency band Δf, this independence is equivalent to random phase shifts between patch contributions at a receiver. As a result, radiation from patches is combined at the receiver in terms of energy, not amplitude, and angular directivity is greatly reduced. In these studies, the question of rupture kinematics was ignored. As a next step, Gusev & Pavlov (1991) introduced space–time (HF luminosity), that is time-dependent energy flux from unit fault element, within the frequency band Δf. Making a fault patch to radiate energy, not amplitude, results in incoherence automatically. Whereas such an approach works well for synthesizing scenario earthquake time functions (Gusev & Pavlov 2009; Gusev 2011), it, being phenomenological, sheds no light onto the physical origins of incoherency.

In this context the note of Boore & Joyner (1978) should be mentioned, that to form incoherence, non-monotonous growth of rupture front in space–time might be relevant. Day *et al.* (2008) further developed this idea. To implement it in sufficient detail is the main intention of this paper. This is far from trivial, as traditionally an earthquake source is treated as a brittle shear crack with smooth front geometry. In uniform elastic medium, after nucleation, dynamically growing crack accelerates and, in the realistic case of planar crack, approaches some limiting velocity close to (or even in excess of) shear wave velocity c_S. Despite the existence of limiting velocity, local variations of rupture velocity, and related disturbances of the shape of rupture front can be expected, caused, for example, by local variations of fracture energy.

Perrin & Rice (1994) performed a linearized perturbation analysis of propagation of planar crack (with initially straight front, and with uniform velocity) after entering into a zone of non-uniform fracture energy in the crack plane. They found that 'the front of a crack that can run forever in a random unbounded medium grows overwhelmingly wavy'. Perturbed behaviour is predicted also for front velocity. Although these results were developed for Mode I crack, generalization of their qualitative aspects to shear cracks seems permissible. Also, Fineberg & Marder (1999) note that fracture energy depends on front velocity and that inverse statement is also true. These results support the accepted concept of randomly varying local rupture velocity depending on variable resistance to crack tip propagation.

The analytical approach, being accurate, does not permit to follow up the developed stages of random rupture. Convoluted space–time geometry of rupture front was proposed qualitatively in Gusev (2013) and was then illustrated by kinematic simulation in Gusev (2014; further abbreviated to G14). Gusev (2013) looked for a model that would explain low HF directivity, and assumed that real earthquake rupture has 'lacy' geometry and, in general, represents a multiply connected fractal line (polyline).

To clarify the point let us introduce a convenient analogy of an instant rupture front in the form of a coastline of a land mass gradually flooded by raising sea level. Assume the land ground to be permeable for sea water, so the surface of any lake is at sea level. Increasing the degree of irregularity of land relief, various kinds of coastline can be formed: from simple continuous beach to tortuous cape-and-bay forms, to, finally, multiply connected coasts ('skerries'). In the last case, islands, left in the rear, correspond to high-strength/low stress unbroken patches of a fault, whereas isolated lakes appear landward from the main coast, representing distantly excited fault patches. Generally, such a complex front occupies a strip of finite width, further called 'front strip'. The simplest case of an even beach corresponds to the common concept of smooth shape of rupture front. Lake-like features of rupture growth were found in theoretical modelling (Day 1982) and in real earthquakes. For instance, Archuleta (1984) and Spudich & Cranswick (1984), using different input data sets, revealed a real jump of rupture front when performing inversion of near-source records of Imperial Valley 1979 earthquake. As for island-like features, I know no direct evidence regarding them, but they must be common in the form of immediate or short-delayed aftershocks; these are not well observable but highly probable.

Based on this 'geographical' analogy, in G14 a simple model of geometry of a 'lacy rupture front' was proposed. Initial step of its construction is a regular smooth line moving in space–time, which described evolution of the average front. This space–time construct was then perturbed by adding extra delay at each point. This perturbation was conceived, and then simulated, as random self-similar field with certain rms amplitude. Through controlling the perturbation amplitude, all described coastline variants could be reproduced, from smooth to convoluted single-connected to multiply connected, evidently fractal. Simultaneously, the width of front strip, w, defined through rms deviation of the front from its unperturbed shape increased, following the increase of perturbation amplitude. Random front geometry was combined with random field of local stress drop. With these two independent and interacting random components combined, this model was labelled 'doubly stochastic source model' or DSSM. This model permitted to reproduce successfully the three key qualitative properties of the high-frequency (HF) earthquake radiation: flat acceleration source spectrum, distinct second corner frequency at $f = f_{c2}$, and the diminution of directivity at HF.

A significant property of the G14 model was the linear relationship between w^{-1} and f_{c2}. This concept departed from the notion of 'slip patch' (Boatwright 1988), or a free-slipping patch on the fault adjacent to a failed fault element. Over this patch, the fault-guided waves, mostly Rayleigh waves, can propagate, and the distance of their propagation defines the duration of elementary displacement pulse radiated as body wave by a fault element, in a certain generalization of Das & Kostrov (1986). Two assumptions were made in G14: first, that the mentioned propagation distance is defined by the front width w_{fr} (with its value on the order of 3 w), and that the duration of the mentioned wave pulse, proportional to w_{fr}, defines the value of f_{c2}. The approach of G14 will be substantially used in the following, in particular for numerical estimates. Still, the success of this approach was only limited as 'lacy' fronts arose within it in an *a priori* manner. Of evident interest are physical processes that may form the lace-like geometry.

It should be mentioned that notwithstanding the fact that the close connection between w and f_{c2} claimed in G14 is in essence a plausible hypothesis, this hypothesis finds a quite good support in otherwise enigmatic anomalous scaling of f_{c2}. This anomaly is evident when one compares scaling of the common corner frequency, $f_{c1,}$ and of f_{c2}. Both mainly follow the rule of the kind $f_{ck} \propto M_0^{-\beta_k}$; however β_1 and β_2 differ. Whereas for f_{c1}, $\beta_1 \approx 1/3$, as could be expected from the assumption of similarity of earthquake ruptures, the increase of f_{c2} with magnitude is much slower (Gusev 1983); observations give values of β_2 in the range 0.16–0.27 (see Gusev 2013, for a review; for fresh well-established results see Archuleta & Ji 2016 and DeNolle & Shearer 2016). This phenomenon was qualitatively explained in Gusev & Guseva (2016) by the analogy with well-known scaling of front width in random growth phenomena. Denote source length as L; then the front propagation distance R is (0.5–1)L. In the simplest, 1-D, case, evolution of front width is described by the classical theory of 'random walk with drift' (Feller 1957) which predicts simply $w \propto R^{0.5}$; thus $\beta_2 = 1/6$. The 2-D case is more complicated, still the values of β_2 significantly below 1/3 can be expected.

Generally, I know no solid explanation both for formation of f_{c2} and for plateau in acceleration spectrum at frequencies above f_{c2}. Modem textbooks (Shearer 1999; Stein & Wysession 2003) relate f_{c1} and f_{c2} to durations of two box-car time functions describing, one, propagation of dislocation at a constant speed, and another, time history of dislocation growth at a point. The plateau in an acceleration spectrum (i.e. the ω^{-2} type of displacement spectrum) is then formed through convolution of the two boxcars, each with ω^{-1} HF asymptotes, and, conceptually, this is reasonable. When taken at the face value however, such a model is unsatisfactory, predicting unrealistic acceleration time histories consisting of only four delta-like singularities. One can try to smooth such time history, but this will immediately destroy the target asymptotic behaviour of ω^{-2} type. Dynamic models of a crack, either brittle (Madariaga 1977) or with cohesive zone (Kaneko & Shearer 2014) provide more consistent explanation. The cases of crack-like and slip-pulse–like propagation were recently analysed in more detail by Wang & Day (2017). However, in all these models, slip terminates abruptly or nearly abruptly along the crack border, whereas seismogeological data (Scholtz & Lawler 2004; Manighetti *et al.* 2005; Wilkins & Schultz 2005) as well as most slip inversions collected in SRCMOD (Mai & Thingbaijam 2014) suggest smooth termination of slip function along periphery of a real earthquake fault. Including this feature into the crack model would again add supplementary smoothing of source time functions, undesirable when one pursues explanation of ω^{-2}. To put this other way, the HF behaviour of source spectra seem to be formed rather during perturbed propagation of rupture, caused by fault heterogeneity (Madariaga 1977) and not at its stopping; corresponding 'stopping phases' are practically not discernible at HF.

There are two main approaches to description of this fault heterogeneity: either through individual features—barriers and asperities—or, more adequate for our aims, through a random field. Andrews (1980) proposed to treat fault heterogeneity as random self-affine (generalized self-similar) random field, that is one with power-law mean power spectrum $S(k) \propto k^{-2\delta}$. where $k = (k_x{}^2 + k_y{}^2)^{0.5}$ is the length of wavenumber vector. If $S(k)$ describes stress drop, and $\delta = 1$, then the stress drop field is self-similar (narrow sense); at other values of δ it is self-affine. At $\delta = 0$ the field is 2-D white noise, that is uncorrelated. Andrews' guess regarding self-similar stress drop field was confirmed to a large degree by the study of inverted slip distributions (Tsai 1997; Somerville *et al*. 1999; Mai & Beroza 2002). Boatwright & Quin (1986) incorporated this concept into elastodynamic rupture simulation; they assumed power law 2-D spectra both for initial stress and for strength. They found important features of such models like sub and super-sonic local rupture velocities, and irregular rupture fronts. This line of study was further developed for more complicated models (see e.g. Dunham *et al*. 2011). Also, computationally faster techniques of pseudo-dynamic simulations of heterogeneous ruptures has been developed (Guattieri *et al*. 2004; Song *et al*. 2014; Crempien & Archuleta 2015). Unfortunately, the problem of high-frequency directivity are not discussed in these papers. As regards relationship between random fault and random radiation, Herrero & Bernard (1994) noted that a jump-like dislocation sweeping a fault with self-similar stress drop field produces ω^{-2} spectrum, a highly instructive property.

An important point is whether functions, which represent slip, stress, etc. over a fault, should be assumed to contain energy at all scales, or some characteristic length, and specifically lowermost intrinsic scale of the fault, should be introduced, larger than the spatial step prescribed within a numerical simulation. In their instructive paper, Ben-Zion & Rice (1993) introduced a consistent model of quasistatic rupture in elastic body, with numerical cell size much smaller than that of possible physical cell size ('segmentation length' or 'coherent slip patch size'). Similarly, Madariaga & Olsen (2002) speak of a 'minimum slip patch'. In mechanics, this viewpoint was originated by Novozhilov (1969); also Morozov & Petrov (2002) speak of 'quantum nature of fracture dynamics'. Observations, which suggested a characteristic small size of seismically active crust, were presented by Chouet *et al.* (1978). They worked with three data sets of small earthquakes from different locations, and, analysing their source spectra, found indication of a well-expressed minimum source size of such an earthquake; this size occurred to be specific for each of the three zones. A good independent example of this kind was given in Sacks & Rydelek (1995) and Rydelek & Sacks (1996; further both referred as SR95) who developed on this basis their concept of 'earthquake quanta' which form a network of cells over fault area. For a particular earthquake fault; there exists also the uppermost intrinsic scale, somewhat smaller than earthquake size (Somerville at al. 1999; Mai & Beroza); this point, being important in general, is of low relevance here, and is not accounted for while simulating random fields over a fault.

Another manifestation of finite size of fault inner structure was perceived by Papageorgiou & Aki (1983) and Gusev (1983) in the existence of the upper cut-off of source acceleration spectrum of a large earthquake, commonly called 'source-controlled $f_{\max}$' and denoted here for brevity as f_{c3}, for 'third corner frequency.' Despite long controversy, its existence (despite masking effect of 'site-controlled $f_{\max}$', at present often discussed in terms of κ_0) is supported by increasing amount of evidence; see review in Gusev (2013). The typical range for f_{c3} is 4–15 Hz, with slow decrease with magnitude, suggesting characteristic size of 100–300 m. Aki & Jin (2000) call this parameter 'inner fault scale'. Perrin & Rice (1994), in essence, also introduce characteristic length of fault surface, which corresponds to their characteristic distance between multiple small asperities.

The model developed further has some properties common to the approach of SR95. In their model, following Burridge & Knopoff (1967), failure of a cell loads a neighbour cell, and may initiate its failure. Cells interact through elastic field; failure is ruled by dry friction; cell strengths are random uncorrelated (white 2-D noise). Slip of a failed cell is local, ruled by local stress. To permit slip at a point of the fault to grow with fault size (and magnitude), a cell can fail repeatedly if reloaded by stress redistribution caused by failures of neighbour cells. Example rupture simulated in SR95 shows, on a snapshot, a front-like feature, of relatively narrow width, which consists of multiple failing cells. Still, no picture is given in SR95 of a front line (single or multiply connected); examples are given only of instantly failing cell clusters but do not represent a distinct boundary. Radiation formed by this model was not considered.

Another cellular model, particularly aimed at explaining HF radiation, is one after Lomnitz-Adler & Lund (1992). They depart from the notion of percolation. A sequence of failures propagates over a grid of cells. Consider a particular unbroken cell A. If a cell breaks in its neighbourhood, cell A can be 'infected', and break, with certain probability $P < 1$, or alternatively can be converted into the barrier state, with probability 1–p. In such a process, permanent lacy geometrical structure ('lacy cloth') is formed, in difference with G14 where only short-lived 'lace fringes' appear. Over the completed 'lacy cloth', a constant-slip circular dislocation line propagates, and HF radiation is formed when the intermittent random sequence of active and barrier cells is crossed by the front. The model is instructive but doubtful, as it is in contradiction with seismogeology: along a continuous fault (with no stepovers), the observed fault slip never abruptly stops and appears again within a short distance.

To summarize, one can believe that an attempt to apply cellular model for the description of formation of 'a lace' at rupture front may be meaningful, and eventually may permit to simulate HF radiation. Note that cellular models are conceptually very simple: each cell is a simple automaton ruled by the same algorithm. A complicated behaviour of a grid of automata, and of random fronts in particular, can appear by supplying automata with non-identical numerical parameters.

Last decades, formation of random fronts in various non-stationary natural and engineering processes was widely discussed and modelled, comprising a considerable research field (see e.g. Halpin-Healy & Zhang 1995; Gouyet 1996; Bonamy 2009, for reviews). These studies can provide useful analogies for rupture fronts in an earthquake source. The following study objects can be listed, among others:

(1) *Single-connected fronts with random geometry:* surface growth; sedimentation; surface etching; imbibition of liquids into a porous material, growth of bacterial colonies and of tumours;

(2) *Multiply connected fronts*: slow crack front propagation, non-detonation explosion of a gas cloud (deflagration), solid propellant burning in a rocket motor, evolution of a (real) forest fire.

The latter process provides most direct analogy to propagation of earthquake rupture; it was often analysed using cellular models. For a forest fire, formation of 'islands' (slowly burning or unburned patches in the rear of the front) is common. Also jumps of front forward ('lakes') are often formed, by brands blown downwind.

An important issue is testing the model against observations. There are earthquake parameters that can be used for this aim. First, it is the width of rupture front. The hypothesis of linear relationship between $1/w_{fr}$ and f_{c2} was already mentioned above. SR95 and G14 associated rupture front width w_{fr} of their models with slip pulse width l of Heaton's (1990) fault model. Still, this is far from being certain that it is l that manifests itself in f_{c2}, and not directly w_{fr}. At any rate, these views differ from those of Papageorgiou & Aki (1983, 1985) and Aki & Jin (2000) who associate f_{c2} with the second, larger inner fault scale, which they relate to the characteristic between-barrier distance. A useful dimensionless parameter related to w_{fr} is the rate λ of its growth with earthquake size L. Assuming plain similarity of earthquake sources, w_{fr} must be proportional to L: $\lambda_L = \frac{d \log w_{fr}}{d \log L} = -\frac{d \log f_{c2}}{d \log L} = 1$. For sets of observed spectra, λ_L is significantly below unity (Gusev 1983), with typical $\frac{d \log f_{c2}}{d \log L}$ in the range -(0.5–0.8). (Atkinson 1993; Gusev 2013; DeNolle & Shearer 2016). Scaling of the kind $\frac{d \log w_{fr}}{d \log L} < 1$ is a good indicator of random growth (Gusev & Guseva 2016). Another, more common, parameter, which can be used for comparing real and simulated ruptures, is average rupture velocity.

In the present work, a cellular model of formation of propagating 'lacy fringe' is developed that hopefully catches the physics of earthquake rupture formation better than *a priori* construction of G14, though the model is again of the double-stochastic kind. A mechanism for formation of random front will be discussed, and properties of synthesized fronts will be compared to those of real faults. Generally, such comparison might yield some estimates of parameters of the developed cellular model. However, the number of possible significant parameters of the model is larger than the number of observational constraints. This prevents constructing any complete description. The goal of this study is mostly the demonstration of a concept. Although the entire presented numerical analysis uses some fixed guesses, I hope that at least the order-of-magnitude estimates of model parameter can be obtained.

The general organization of the paper is as follows: (1) description of algorithms and parameters comprising the cellular model; (2) illustrations of properties of the cellular model by examples, observing how variations of numerical parameters affect the behaviour of the model; (3) systematic scanning of parameter space and determination of verisimilar intervals of parameters and (4) running the procedure for synthesis of (uncalibrated) accelerograms, with front kinematics simulated by means of the cellular model. The front history obtained in this way is combined with the random field of local stress drop, like in G14. In this manner, waveforms and their spectra are obtained. These spectra indeed manifest the above-described characteristic features, of second corner frequency and of acceleration spectrum plateau. Also, the finiteness of cell size results in formation of f_{c3}.

2 A KINEMATIC CELLULAR MODEL OF EVOLUTION OF EARTHQUAKE RUPTURE

2.1 The background of the suggested model and requirements it should fulfil

The classical dynamic model of an earthquake source rupture is a shear crack in brittle elastic body, which propagates spontaneously under the effect of shear stress. In difference with the general case, fault-crack is channelized and mostly follows a certain weak plane defined by a geological fault. The crack tip plays the role of rupture front. The following properties of crack formation are especially important.

(1) Crack tip propagates spontaneously when the critical (Griffith's) size of a crack is exceeded. See theoretical results reviewed for this case in Rice (1980) whom I mostly follow. After initial acceleration, asymptotic velocity of a model crack is c_S for Mode III and $v_R \approx 0.9c_S$ for Mode II. Also, the theory (Andrews 1976 and later work) describes the possibility of propagation of Mode

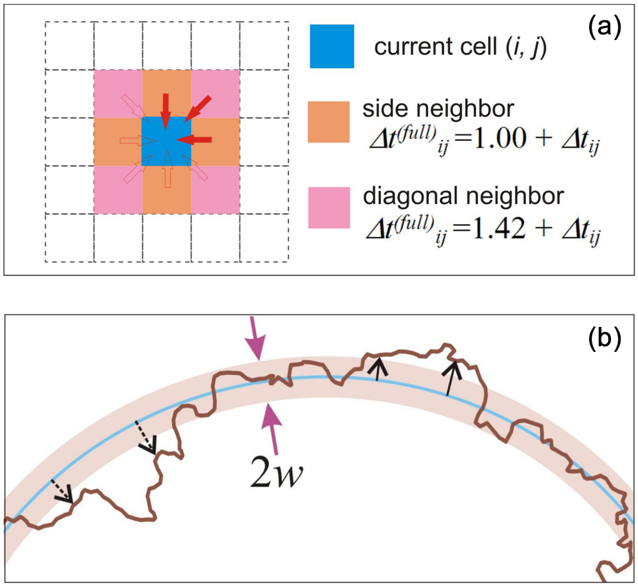

Figure 1. (a) A cartoon showing a cell and its neighbours. Filled arrows are from cells, which tried to initiate the I→F event in the current cell (to 'ignite' it). In any of neighbour cells, this attempt occurs at the moment of F→B event in this neighbour cell. Among these, the successful is one with the earliest time of its F→B event. Empty arrows are from other cells, which also can ignite the current one, but only potentially. (b) A sketch illustrating definition of rms front width, *w.* Positive and negative individual deflections of the actual front line (corrugated brown) from the ideal, no-resistance front line (blue arc) are depicted as solid or dashed arrows. Deflections are measured along local normal to unperturbed front. To find *w,* root mean square deviation of deflections is calculated; the $\pm\ w$ strip is schematically shown. The assumed actual front width is $w_{fr} = 2.5\ w$.

II crack at velocities above c_S. In this mode, separate ('lake-like' in terms of Introduction) secondary cracks with high 'intersonic' ($c_P > v_r > c_S$) velocities nucleate under the effect of the dynamic stress field formed by running 'subsonic' ($v_r < c_S$) rupture. In agreement with the theory, average velocities of rupture propagation observed in earthquakes are usually in the range (0.5–0.9)c_S, and cases are systematically found when local velocity exceeds c_S.

(2) Local random variations of resistance to fracture propagation can be expected. These variations can reflect: non-uniform material parameters, like fracture energy; wavy profile of fault walls and of entire fault; fault bifurcations or small kinks, etc. Such variations of resistance cause deviations of local rupture front velocity from a constant. As a result, the front shape is distorted, and rupture velocity varies. To formally describe distortions of front shape, one can introduce the notion of rms width *w* of the front, defined as standard deviation of actual instant front position from its unperturbed or mean position, with deviations measured across the unperturbed front (Fig. 1). See Introduction for short presentation of the work of Perrin & Rice (1994), who accurately treated the linearized case of small perturbations of resistance.

(3) Front of a crack has no inertia (Madariaga 1977; Rice 1980, eq. 5.39 and further) and is therefore capable to bend sharply around obstacles.

Justification for introducing a cellular model of rupture front is given in Introduction. Such a model should reproduce the listed properties whenever possible; but some simplifications will be made. In particular, the difference between velocity limits for Modes III and II is neglected, and a fixed isotropic upper bound is set for front velocity, assumed equal to c_S. The possibility of larger velocities is ignored. In the present simulation, rupture velocities v_r are normalized to the upper limit, c_S, giving normalized velocity, or (*S*-) Mach number $m = v_r/c_S$, always below unity here. In the following, *m* will be called velocity for brevity. The key check for the developed model is its capability to reproduce properties of fronts of real earthquake ruptures. In particular, as mentioned in Introduction, I try to reproduce scaling of rms width *w* with earthquake size, and rupture velocity. Also, it is interesting to check the capability to reproduce the HF features of real sources already emulated in G14.

2.2. The general structure of the model

The present model is constructed taking into account the listed requirements. It consists of a $N \times N$ grid of square cells filling a part of a plane. In each cell, an elementary automaton is located. All automata are qualitatively identical, but their parameters vary from cell to cell. An automaton has three states. The transition between states occurs in continuous time. (The well-known 'cellular automaton' class of models is different—within it, time is assumed discrete, not continuous.)

Let us consider the rules that control an automaton. Traditionally, *input* variables for choosing a transition of an automaton are the states of neighbour cells. An equivalent approach, more convenient here, is to describe automaton in a cell through its eight *outputs* or commands sent to each neighbour. Which command to choose depends on states of the automaton and its neighbours. Generally, a random element can be used in formation of a command; however, the variant of the model with random commands is only tried here; this line is not developed in any depth. In the main part of this work, the model rupture develops spontaneously in deterministic mode. However, this evolution occurs over a random landscape: properties of each individual cell are random, and are preset before evolution begins ('quenched heterogeneity').

2.3. Grid of cells and time count

On a plane (*x, y*), a grid of square cells is located with centres at $\{x,y\} = \{i\Delta x, j\Delta y\}$; $i = 1,2, \dots N$; $j = 1,2, \dots N$. Let $\Delta x = 1$ and $\Delta y = 1$; and let us use as the time unit the time for an unperturbed rupture to propagate along a side of a cell. Consider a cell and its eight neighbours (Fig. 1a): four side neighbours at locations (i, $j \pm 1$) and ($i \pm 1, j$), and four diagonal neighbours at ($i \pm 1, j \pm 1$). Denote full rupture delay between failures of the central and any of the neighbour cells, $\Delta t^{(f)}{}_{ij}$, as

$$\Delta t^{(f)}{}_{ij} = \Delta t_o + \Delta t_{ij} \tag{1}$$

where Δt_o is pure propagation delay, fixed; and Δt_{ij} is random additional delay. Δt_o equals 1 for a side neighbour and 1.414 for a diagonal neighbour. The set of Δt_{ij} is a 2-D discrete random field over the grid; its construction to be specified. It reflects local fault resistance to rupture propagation. In terms of velocity *m*, in the ideal case of $\Delta t_{ij} = 0$, the value of *m* equals unity along any row/column or diagonal of the grid.

2.4. States of an automaton and the permitted transitions

A cell can be in any of the following states: intact (I), failing (F) and broken (B). The key property of a cell is the value of lifetime for its F state, or delay Δt_{ij}; it is a preset random number. The complete $N \times N$ set of delays is defined by a random seed, unique for each run of rupture evolution, and by two parameters of the model, to be described. Let us describe each state in more detail.

(1) State I. At the start of evolution of the grid, all cells, except the nucleation cell, are in state I. Its lifetime is unlimited. A cell in state I does not issue commands. State I changes: (I → F) on command from a neighbour in state F, at the moment of its (neighbour's) transition (F → B).

(2) State F. At a particular cell (*i, j*), state F arises through the transition I → F by a command received from one of its neighbours. Consider a neighbour of the (*i, j*) cell which undergoes transition F → B at a certain moment t_1. After delay Δt_o, a timer is launched at the (*i, j*) cell ('moment of ignition'). Each neighbour which undergoes the F → B transition tries to launch the timer; but this occurs only once, at the earliest attempt. Later attempts do not work as the cell is already in the F state, and only single I → F transition is permitted. The timer is controlled by the preset lifetime of state F, set to Δt_{ij}. At the moment when the timer runs out, the transition F → B occurs in the (*i, j*) cell. This moment is $t_1 + \Delta t_{ij}^{(f)} = t_1 + \Delta t_{ij} + \Delta t_0$. At this moment commands are issued that control the evolution of each of the eight neighbours. A command issued to a particular neighbour respects its state. For a state I neighbour, the transition I→F is caused. For a state F or B neighbour no command is issued. There is a special option of the simulator, when the I →F transition can be caused in non-deterministic mode, with probability, p_{IF}, below unity. This case is intended to illustrate percolation–style rupture models, soon found to be unrealistic. In the main part of the work, $p_{\mathrm{IF}} = 1$. To initialize model evolution, state F is ascribed to a preselected nucleation cell.

(3) State B. Dead-end state, with no outputs. Its lifetime is unlimited. Borders of the modelling area are created setting them to B state.

Note that despite discreteness of events, model time is continuous; it advances only at the moments of I→F and F→B events.

What is the meaning of Δt_{ij}? Madariaga (1983) classified conceptual models of heterogeneity which determines HF radiation into two groups. There is the 'barrier' group when external stress field does not vary much, whereas fault strength is expressedly non-uniform. In this case, Δt_{ij} may be controlled by this strength: the stronger is the cell (*i, j*), the larger is Δt_{ij}, and the longer is the failure process needed for a rupture to cross it. Another kind of inhomogeneity is the 'asperity' one, when strength variation is less significant whereas local stress is expressedly non-uniform, caused for example by self-stress from previous fault motion (seismic or creep), or by specific external stress field. In this case, high-strength cell may be loaded near to its bearing capacity, and will break with minimum delay; whereas for weaker cells, relative stress may be lower and Δt_{ij} may increase. To describe joint effect of all these irregularity factors, the term 'effective strength' may be used.

2.5. Simulating the field of heterogeneity

The preset table of Δt_{ij} is formed as a realization of discrete random field, which is assumed isotropic and self-affine. Such a realization is easy to generate in the case of Gaussian statistics of Δt_{ij} values. However, a special technique is needed to generate fields with other statistics. The approach I use is 'quantile-to-quantile transform' which is a modification of the Van der Waerden's classical 'normal score' technique. Its common variant, called 'normal quantile transform', is often used in many fields like hydrology, geostatistics and more including seismology (Goda *et al*. 2014), to convert non-Gaussian data into Gaussian quasi-data preserving their rank (often to permit further use of statistical tests developed for Gaussian data). The same approach can be used in the opposite direction converting Gaussian values to non-Gaussian ones, in particular for simulation of self-similar slip map over a fault (Gusev & Pavlov ; Goda *et al*. 2014).

I use this technique to transform a Gaussian field into non-Gaussian field with approximately the same correlation properties. This is done in steps. First, Gaussian random field z_{ij} is generated:

$$z_{ij} \equiv z(x_i, y_j) = DFT\left[z_{pq}(k_{x,p}, k_{y,q})\right] = DFT\left[k^{-\eta}\zeta_{pq}\right] \qquad (2)$$

where $\{x_i, y_j\}$, $i = 1,2,\ldots N$;, $j = 1,2,\ldots N$; is position of a cell, *DFT* denotes discrete Fourier transform, $\boldsymbol{k} = \{k_x, k_y\}$ is wavenumber vector, $k = |\boldsymbol{k}|$, and ζ_{pq} is standard Gaussian random, uncorrelated (delta-correlated). Correlation properties (along x and y) are imposed through the $k^{-\eta}$ factor; at $\eta = 0$ the result is 2-D white noise. Then z_{ij} are sorted, forming variational series $[z_{ij}]_m$, $m = 1,2,\ldots N^2$. For each member of this series, its quantile value $[Q_{ij}]_m = m/N^2$ is found. Consider another, target, distribution law. I particularly used the standard exponential law with cumulative distribution function $E(q) = 1–\exp(–q)$. Consider inverse function $E^{-1}(Q) = \log_e(1–Q)$). It can be applied to $[Q_{ij}]_m$ producing an ordered sequence whose members have standard exponential distribution. As the mean of this law is unity, the desired mean value, τ, of the target distribution is introduced by the additional τ factor. In this way, the set $[\Delta t_{ij}]_m = \tau E^{-1}([Q_{ij}]_m)$ is determined; its values are then sent to their proper positions (*i, j*), forming the sought for Δt_{ij} table. Its correlation properties are approximately the same as those of the z_{ij} field; that is Δt_{ij} is close to a sample (realization) of self-affine random field with mean value τ and power spectrum of the $k^{-2\eta}$ kind. (In the particular exponential law case, the quantile-to-quantile transform is excessive; but the procedure is standard, and is ready for eventual use with other laws.)

The choice of the particular exponential distribution law for Δt_{ij} is a guess. It has single parameter, mean τ; its variance $\sigma^2(\Delta t_{ij}) \equiv \tau^2$. Therefore, a particular realization of the Δt_{ij} field is determined by the two parameters $\{\eta, \tau\}$, and by a particular random seed used to generate the ζ_{pq} set. The exponential law for Δt_{ij} was chosen because properties of this law are appropriate: (1) random values are non-negative, therefore a model rupture can only lag behind the ideal unperturbed front (this property permits 'islands' only, no 'lakes'; it eventually can be rejected to increase realism); (2) probability density function is monotonously decreasing: the larger is delay, the less probable it is and (3) it has no mode (peak), that is a characteristic value, whose meaning would be difficult to explain. Note that for the most common—Gaussian—law, each of these properties is violated. The choice of the exponential law is also partly justified by the fact that the results of simulation based on this assumption show no evident contradictions.

2.6. Effects of inhomogeneity

Random terms added to ideal rupture delays distort the shape of rupture fronts (Fig. 2). Also the order of ignition of cells is perturbed. On Fig. 2, ignition sequences are back traced starting from an arbitrary point on the front. One can see that the larger perturbations are, the more convoluted are ignition traces: they stray more intensively and become longer. Both these factors affect average

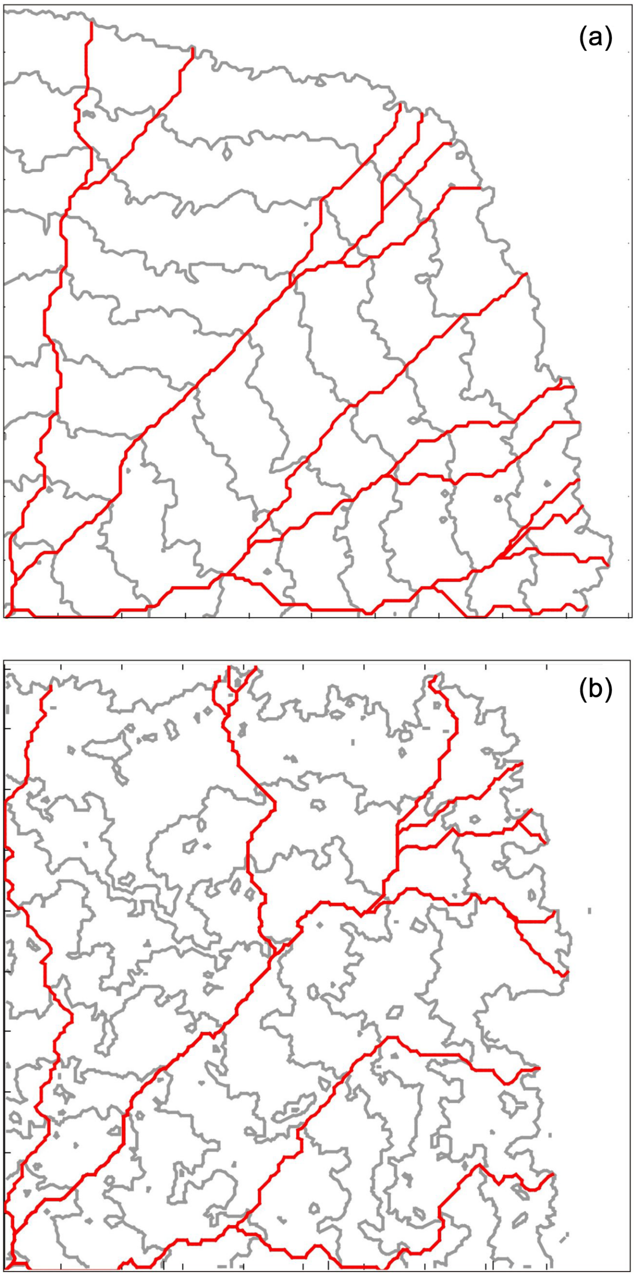

Figure 2. Random space–time geometry of rupture front and ignition paths. (a) Sequential front positions (grey) and several example ignition traces (red). The nucleation point is the SW corner. A case of weak delay perturbations. (b) Like a, more intensive perturbations.

rupture velocity, in addition to the direct effect of additional Δt_{ij} delays.

2.7. Priming and stopping

Generally, model rupture is initiated by a single cell in state F. There is no attempt in the present variant to stop the rupture realistically. Rupture is abruptly stopped artificially when the front touches the preset outer boundary, that is the enveloping square. Such abrupt braking produces artefacts on simulated traces; bypassing this problem is discussed later.

2.8. Parameters to be monitored during rupture evolution

To characterize a particular style of evolution, the following parameters were selected for monitoring.

(1) Front leader propagation distance, r_{fr}, measured in cell units, is the distance from the nucleation point to the most distant point of the front.

(2) Effective instant radius of the source, r_{eff}, is the average distance from the nucleation point to a point of the front. It is calculated as $r_{eff} = (N_B/\pi)^{0.5}$ where N_B is the instant area of rupture defined as the current number of cells in state B.

(3) Rupture velocity, *m*. Two variants of this parameter are used: m_r and m_e. m_r is defined as r_{fr}/t. This parameter can be directly compared to observations. m_e is defined as $m_e = dr_{eff}/dt$, and determined by linear regression over (t, $r_{eff}(t)$) pairs. This parameter gives the average rate of spreading of the front. If the ratio m_e/m_r is close to unity, the front grows isotropically, like a distorted circle; otherwise, if m_e/m_r is much below unity, this may signalize that the front forms significant individual 'tongues' (e.g. as in the case of Fig. 5e).

(4) Root mean square (rms) width of front, *w* (Perrin & Rice 1994; G14). As explained above, *w* is standard deviation of deflection of a point of front from its mean or unperturbed position (see sketch, Fig. 1b). The current front is assumed to consist of all state F cells; both single connected and multiply connected fronts are processed in the same manner. To determine the value of *w* at a particular moment of simulation time, one can use the set of distances of the current random realization of front with respect to its reference position on the octagon. Actual distances are calculated along a ray from the origin to each point of the front. The reference distance, for each value of actual distance, is defined as product of two factors: azimuth-dependent, defined by the known standard octagonal shape, and time-dependent effective rupture radius. To analyse evolution of *w*, it can be considered as a function either of time, or of distance. For tracking evolution of an individual simulated source at fixed parameters τ and η, using $w(t)$ is most appropriate. However for general understanding and for comparison with observations it is also useful to consider $w(r_{eff})$ and $w(r_{fr})$, estimated indirectly as $w(t(r_{eff}))$ and $w(t(r_{fr}))$. For the aims of comparison, the values $w_{t100} = w(t|t = 100)$, $w_{r100} = w(r_{eff}\,|r_{fr} = 100)$ and $w_{r100} = w(r_{eff}\,|r_{fr} = 100)$ are estimated, in the following way. First, $\{t,\ w,\ r_{eff}\}$ triples are accumulated during evolution. Then linear regression of *w* versus *t*, versus r_{eff} or versus r_{fr} is done in log–log scale, and the required values are picked using approximating trends.

(5) Logarithmic growth rate of *w*. It was studied in two variants: $\lambda_t = \frac{d\log w}{d\log t}$ and $\lambda_r = \frac{d\log w}{d\log r_{eff}}$. These are estimated during the same linear regression as described in previous paragraph. Parameters λ_t and λ_r serve as exponents in the growth laws $w \propto t^{\lambda_t}$ or $w \propto r_{eff}^{\lambda_r}$.

(6) Fractal dimension of front, *D,* specifies how complexity of the front increases along with its growth; in other words, how increases its deviation from a smooth 'Euclidean' line. *D* is determined from the relationship L_{fr} versus L_e where L_{fr} is the actual length of the possibly fractal front, and L_e is (imaginary) Euclidean length calculated as $L_e = 2\pi r_{eff}$. The value of L_{fr} is equated to the number of cells in state F; a correction factor is added in order to guarantee $D = 1$ for non-perturbed front. As follows from (Mandelbrot 1982), $D \approx \frac{d\log L_{fr}}{d\log L_e}$. In such calculation, it is supposed that the set of instant states of the growing area of simulated source can be

treated as the set of fractal islands of various sizes, each of them representing possible source contour. Technically, it is convenient to determine $D - 1 \approx \frac{d \log(L_{fr}/L_e)}{d \log L_e}$; this is done through linear regression.

3. EXPERIMENTS WITH SIMULATOR: STYLES OF BEHAVIOUR OF THE MODEL

Let's consider examples of behaviour of the above-described model at some characteristic sets of parameters. All experiments were initiated at the grid centre.

3.1. Introductory examples

The deterministic closed shape of unperturbed front is illustrated on Fig. 3(a). In this reference case of negligible τ, numerical front is octagonal. It grows symmetrically and at a constant velocity. It represents discrete approximation of a spontaneously growing crack of circular shape; its velocity along eight fast directions in this case is close to 0.97.

An example continuous perturbed front is shown on Fig. 3(b). In its generation, the following parameters were used: $\eta = 0.5$, $p_{\mathrm{IF}} = 1$, $\tau = 4$. Rare 'islands' are seen that are formed by abrupt turns of front, which sometimes result in pincer movement. Such islands are transient features; all of these eventually disappear if the time margin permits.

Ring-like, isometric fronts are typical for most simulations with self-similar Δt_{ij} field. However, through admixing extra spectral energy at low wavenumbers, formation of unilateral asymmetric ruptures is easily attained (Fig. 3c). The particular direction of the fast-propagation 'tongue' is random and varies from run to run.

Self-similar Δt_{ij} field combined with 'probability of ignition' $p_{\mathrm{IF}} < 1$ results in percolation-style cases (Figs 3d and e). Now when the front propagates it leaves permanent barriers ('islands') in its rear. Two examples are given for $p_{\mathrm{IF}} = 0.30$ and 0.25. At $p_{\mathrm{IF}} = 0.30$ many small and a few big 'islands' appear in the rear of the front. The degree of irregularity of the instant perimeter is comparable to that of the case of Fig. 3(b). At $p_{\mathrm{IF}} = 0.25$ the front loses clear contour and becomes strongly cut up. Instead of a well-formed sponge-like structure of Fig. 3(d), a shapeless seaweed-like structure appears. Islands in the rear close up, forming a 'lacy cloth'. At $p_{\mathrm{IF}} = 0.25$, in a sequence of Monte Carlo runs, cases are frequent when the growth completely stops; the plotted 'successful' variant was selected after a few attempts. With the further decrease of p_{IF}, down to 0.24–0.23, the growth of front aborts practically always. The critical value of p_{IF}, defined as one which gives 50 per cent chances for front to propagate to infinity at the given set of parameters, is close to $p_{IF} = 0.27$ in this case; it is the so-called percolation threshold for the considered problem.

The last two cases remind the percolation cluster model after Lomnitz-Adler & Lund (1992), mentioned in Introduction. Pertinent criticism of percolation cluster model was given above from a seismogeological viewpoint. Also, within our model, front propagation velocity for percolation cluster sources are unacceptable low (below $m = 0.25$). For these reasons, 'lace cloth' cellular source models with $p_{\mathrm{IF}} < 1$ are not considered further, the value of $p_{\mathrm{IF}} = 1$ is fixed hereinafter, and only 'lace fringe' models like Fig. 3(b) will be discussed.

3.2. Styles of evolution of fronts: variable τ

Further, I try to visualize how the variation of the two parameters, τ and η, affect the behaviour of the model. To generate a series of plots, a set of values of one parameter is combined with a fixed value of another parameter.

In the first series, Fig. 4, one can see the effect of variable τ: $\tau = \{0.63, 1.6, 4, 10, 25\}$ at the fixed $\eta = 0.5$. When perturbations are low (Figs 4a and b) the imprint of deterministic octagonal shape can be noticed. In the series of plots of Figs 4(a)–(e) one can see that with increase of τ, the amplitude of front oscillations increases, and its qualitative character changes. At first, front is a single perturbed curve, and a ray from the origin crosses it once. Then, the curve becomes convoluted, so that in many cases a ray from the origin makes multiple crossings. At last, such behaviour intensifies, making lace-like appearance of front; islands of various sizes appear. In other words, the front structure changes from approximately smooth curve to fractal polyline. Front irregularity is an important feature closely related to formation of incoherent HF radiation (Gusev 2013, 2014); to characterize it I use rms front width w.

3.3. Styles of evolution of fronts: variable η.

A series of plots for fixed $\tau = 4$ and $\eta = \{0, 0.5, 1, 1.5, 2\}$ is shown on Fig. 5. Properties of front in this series are following: at $\eta < 1$ fronts are, basically, isometric, whereas with approach to $\eta = 2$ appreciable angular variations of growth rate arise. One might compare this one-sided development of rupture to the tendency to unilateral growth of real earthquake faults; but this guess may be incorrect. One problem is that when $\eta > 1$, fronts evidently become too smooth. Another difficulty is doubtful λ values, the matter to be clarified later.

4. SYSTEMATICAL STUDY OF VARIANTS OF FRONT PROPAGATION

Let us now perform systematical study of behaviour of the model, with the aim to create the basis for eventual estimation of actual values of parameters from observational data.

4.1. A technique for estimation of parameters of front propagation

Further, the behaviour of some properties of fronts over two-dimensional area of parameters (η, τ) is studied. The zone $\eta > 1$ was ignored, for the reasons explained later. As the significant parameters of rupture I selected the following two: (1) growth rates λ_r and λ_t, and (2) average rupture velocity, m. As a certain digression, also fractal dimension D of front line will be estimated, despite the absence of observational data to match. Figs 6 and 7 illustrate the process of estimation. The plotted linear trends were determined based on pooled data of 25 Monte Carlo runs. For visibility, only single variant on each plot is supplied with data points, with significant decimation of samples along abscissa, and only for five Monte Carlo runs.

Plots of Fig. 6 show the relationships log w(log t) and log w(log r_{eff}) for two cases: fixed $\tau = 4$ and variable η (Figs 6a and b); and fixed $\eta = 0.5$ and variable τ (Figs 6c and d). In this and other cases, discreteness produces instability at small t, therefore linear regressions were performed over the t range $[10, t_{final}]$ and the

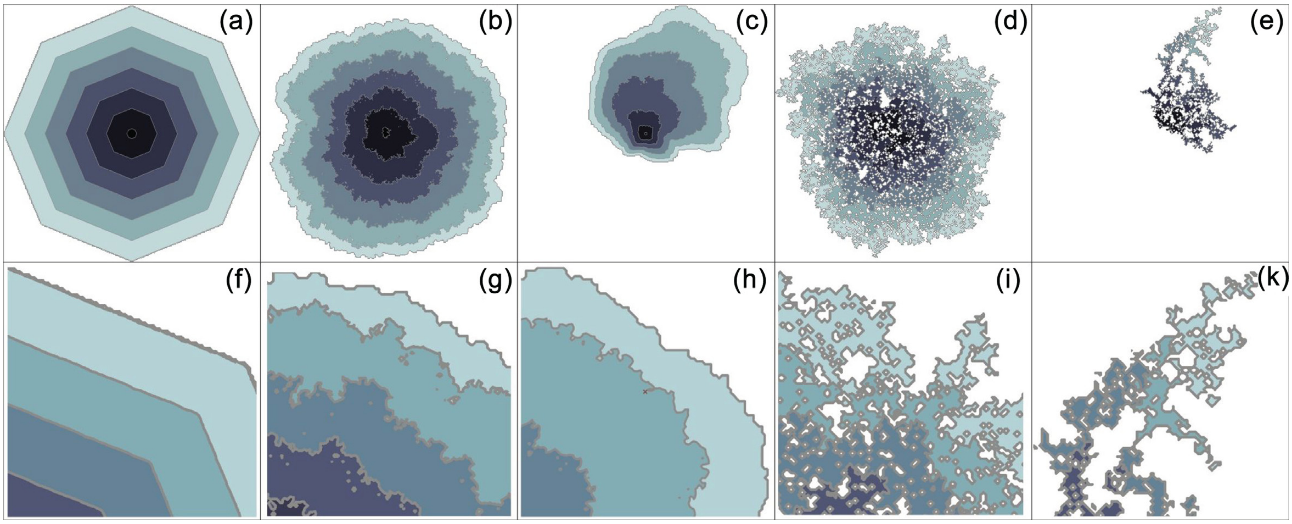

Figure 3. Examples of space–time history of simulated rupture front. Hereinafter on such plots, the shade of grey codes time of transition of a cell into the final state B: the later, the lighter. $\eta = 0.5$ is fixed. *a*—the reference case, obstacles are practically absent ($\tau = 0.05$). In the four following examples $\tau = 4$ is fixed. *b*—a typical case of 'lace' fronts obtained with self-similar Δt_{ij} field and $p_{IF} = 1$. *c*—a self-similar Δt_{ij} field like one in *b* is modified by addition of low-wavenumber component; this results in formation of tongue-like shape. In a particular run, rupture propagation becomes unilateral, though when considered over many runs, its direction is random. *d, e* Δt_{ij} field is self-similar; values of 'probability of ignition' are $p_{IF} = 0.30$ and 0.23, correspondingly. Top row *a–e* is complete picture; lower row *f–k* shows a zoomed fragment of each upper graph, here and in Figs 4 and 5. The grid 300 × 300 is used here and in Figs 4–7.

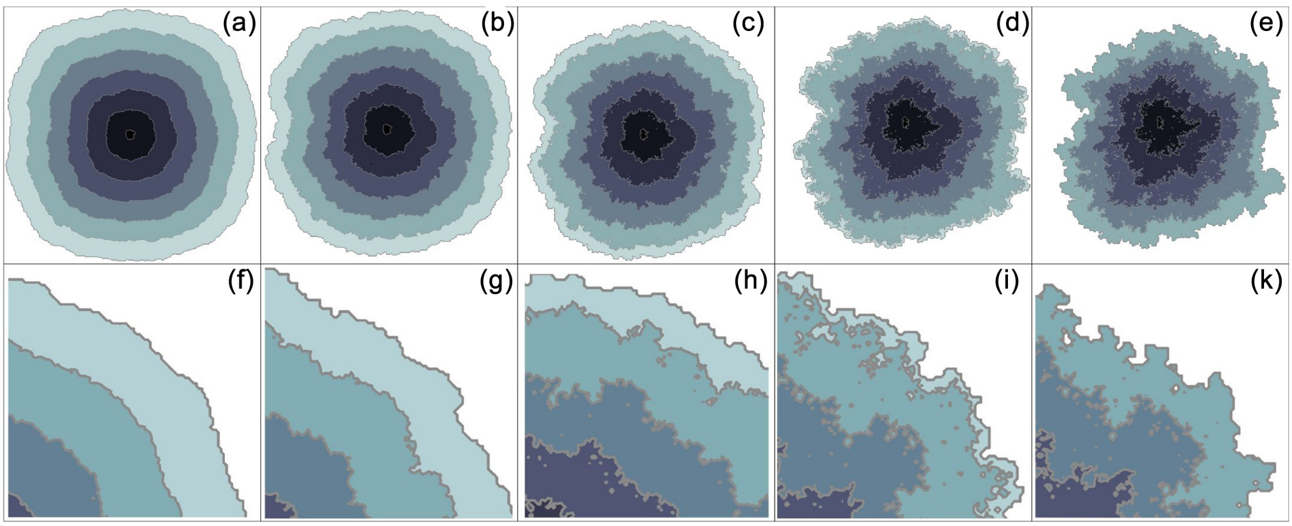

Figure 4. Examples of space-time history of simulated rupture front. Hereinafter on such plots $p_{IF} = 1$. Spectral exponent of heterogeneity is fixed: $\eta = 0.5$. Mean delay τ which controls the degree of heterogeneity varies; $\tau = \{0.63, 1.6, 4, 10, 25\}$ for plots *a* to *e*. Same seed is used for all pictures.

corresponding r_{eff} range. The discussion of the revealed tendencies is postponed to the following section.

Plots of Fig. 7 illustrate determination of m, and of fractal dimension D, they are organized in the same manner as those of Fig. 6. On Figs 7(a) and (b), the case of fixed $\tau = 4$ and variable η is illustrated. On Fig. 7(a), the r_{eff} versus t dependence is shown; slopes of the lines give the estimates of m. Fig. 7(b) shows the dependence of the ratio log (L_{fr}/L_e) on log L_e, the slope of a linear segment yields the estimate of D–1. On Figs 7(c) and (d) the case of fixed $\eta = 0.5$ and variable τ is illustrated in the same manner as in Figs 7(a) and (b). From these plots one can see that m is almost insensitive to variation of η but varies expressedly with τ.

4.2. Simulations for systematic coverage of parameter space

In the manner shown on Figs 6 and 7, variation of rupture parameters over entire investigated area of η and τ was studied. The following discrete grids were used: $\eta = \{0, 0.25, 0.5, 0.75, 1\}$ and $\tau = \{0.63, 1, 1.6, 2.5, 4, 6.3, 10, 16\}$. The values $\eta < 0$ ('blue spectra') are physically improbable and were not examined. Also, the values $\eta > 1$ were not examined for the reasons explained later. Obtained relationships are given in the graphical form on Figs 8–11. To obtain stable numerical estimates, simulations were repeated in $N_{MC} = 1000$ Monte Carlo tries; parameters were calculated for each run and then averaged. On plots, standard deviation of *individual* Monte Carlo estimates is given in many cases; it illustrates the scatter of individual values for various realizations/events. The

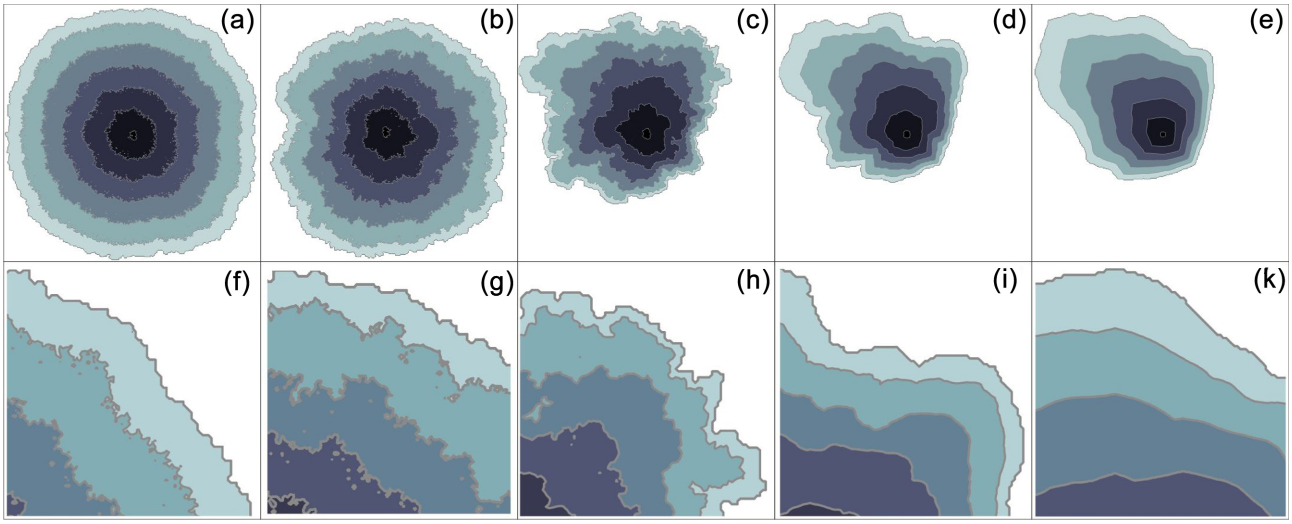

Figure 5. Similar to Fig. 4. Now $\tau = 4$ is fixed, and variants differ by the value of η: $\eta = \{0, 0.5, 1, 1.5, 2\}$ for plots *a* to *e* and *f* to *k*.

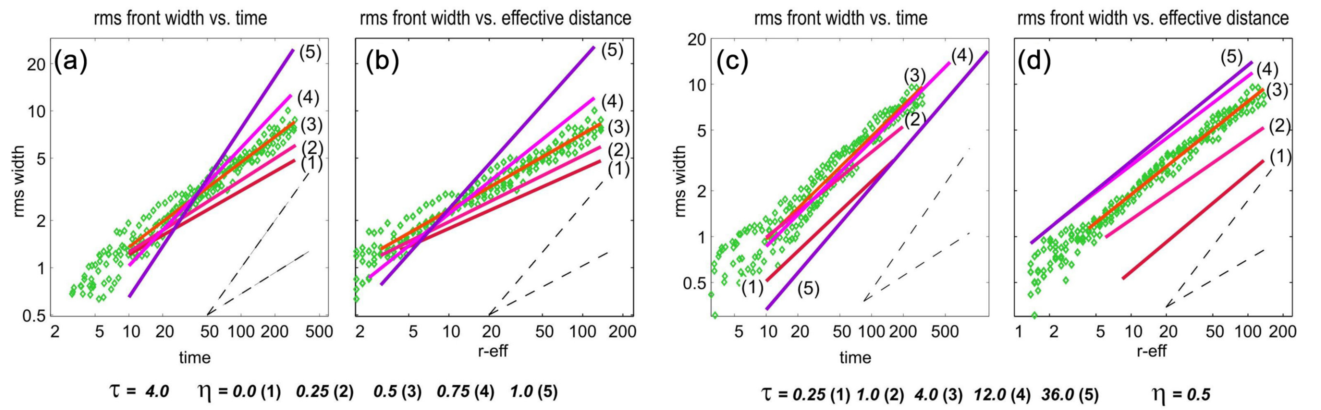

Figure 6. Illustrations for procedures of determination of rupture parameters. (a) Estimation of $\lambda_t = \frac{d \log w}{d \log t}$ for fixed $\tau = 4$ and $\eta = \{0, 0.25, 0.5, 0.75, 1\}$. Straight segments for each value of η are obtained through linear regression over data simulated in 25 runs. Dots are w estimates for $\eta = 0.5$ obtained in five Monte Carlo runs. Dashed lines with slopes 0.5 and 1.0 are guides for eye. (b) Similar to *a,* for $\lambda_r = \frac{d \log w}{d \log r_{eff}}$, (c) similar to *a*, for fixed $\eta = 0.5$ and $\tau = \{0.25, 1, 4, 12, 36\}$; dots are for the case $\tau = 4$. (d) similar to c, with argument $r_{eff.}$

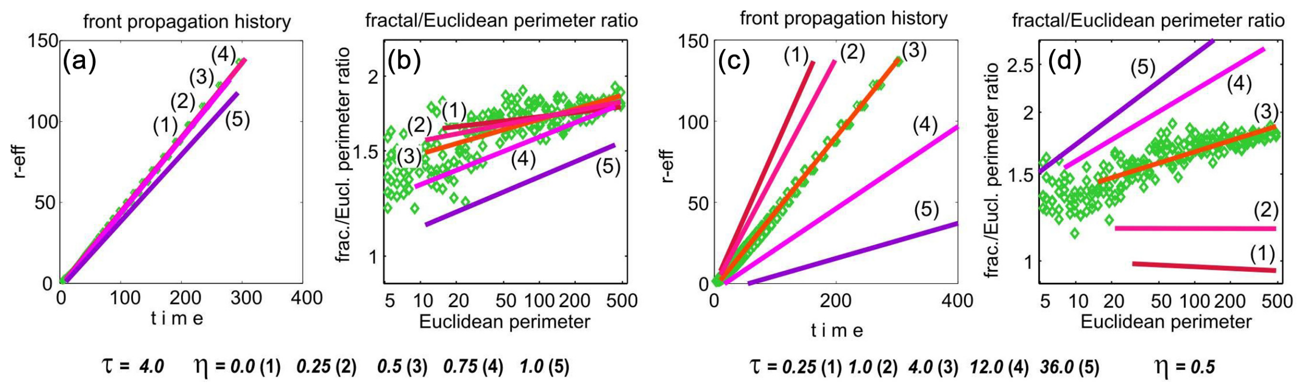

Figure 7. Illustrations for procedures of determination of rupture parameters, continued. (a) Estimation of $m_e = r_{eff}/t$, for fixed $\tau = 4$ and η from 0 to 1. Dots are m estimates for $\eta = 0.5$ obtained in five Monte Carlo runs. Straight lines for each value of η (as indicated at the bottom) are obtained through linear regression over data simulated in 25 runs. (b) Estimation of D-1 $= d \log (L_{fr}/L_{Eu})/d \log L_{Eu})$ performed in similar manner. (c) Analog of *a*, for fixed $\eta = 0.5$ and τ from 0.25 to 36.(*d*) Analog of *b*, for fixed $\eta = 0.5$ and τ from 0.25 to 36. Negative slope of line 1 on plot *d* is an artefact of numerical estimation of D when D is very near to unity.

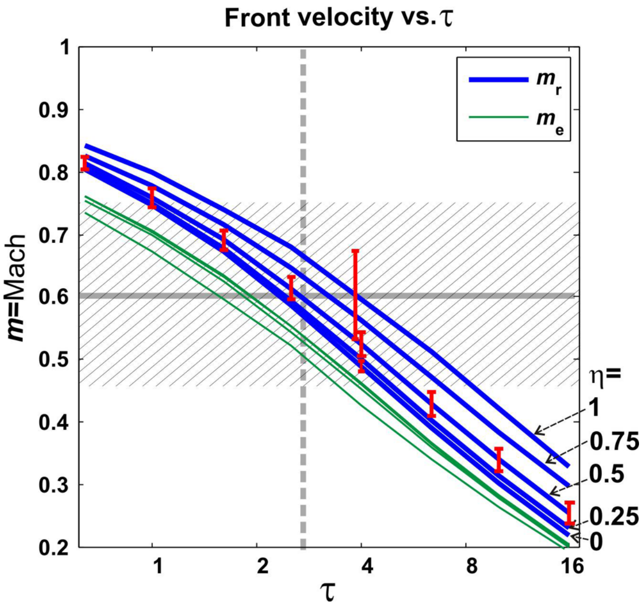

Figure 8. Relationships $m_r(\tau)$ and $m_{eff}(\tau)$ for a number of η values. Here and on further three figures, vertical bars at a curve show standard deviations of *individual* Monte Carlo estimates. Here, bars are given for the curve with $\eta = 0.5$, for several τ values; similar bars are also added for $\tau = 4$ and marginal values of η. The hashed area indicates the approximate range of observed m values and the grey line is the observed reference value (hypothetic average) fixed at $m = 0.60$; see the Appendix for details. Dashed vertical line marks the tentative estimate of the typical $\tau = 2.5$. Although the curves look quasilinear at a first glance, at closer examination a suspicious double bend (very stretched 'S') can be noticed. By using the log–log scale, such a feature can be excluded, however at the cost of pronounced curvature.

rms error of the plotted average trends is ${N_{MC}}^{0.5}$ (≈ 30) times lower. The general mode of presentation is as follows: average parameters are presented as functions of τ, with a particular η value serving as the parameter of a curve.

Fig. 8 illustrates the behaviour of m_r and m_e. On the selected log–log scale, a clear monotonous negative trend versus τ is seen. Two causes of the simulated trend are seen. One is the trivial increase of delays at each propagation step, directly controlled by the value of τ. Another factor is the convoluted propagation path, with steep turns of local discrete propagation trace, more and more common as τ increases (Fig. 2).

Dependence of m_r on η is weak; for m_e it essentially disappears. The cause of this difference seems to be the fact that at larger η, angular variations of front shape increase: compare Figs 5(b) and (d). Then, m_r is determined by an individual particular 'fast tongue' of the front, with its other parts lagging behind; whereas the m_e value is the average over all directions. Weak dependence of m_r on η means that this theoretical plot is useless for deriving estimates of η from observations. Oppositely, if even broad *a priori* bounds are set for η, one can well estimate τ from observed m_r at least approximately.

An interesting point is the scatter of individual Monte Carlo estimates, which may well reflect real scatter related to randomness of structure of individual faults at given τ. This scatter (in logarithmic scale) is almost independent of τ, but grows with η very fast.

Fig. 9 shows λ_t (τ) and λ_r (τ) relationships. These relationships are not identical, but are qualitatively comparable. As seen here, the values $\eta > 1$ seem to cause physically highly improbable $\lambda > 1$ (front width grows faster than rupture size). Therefore only the

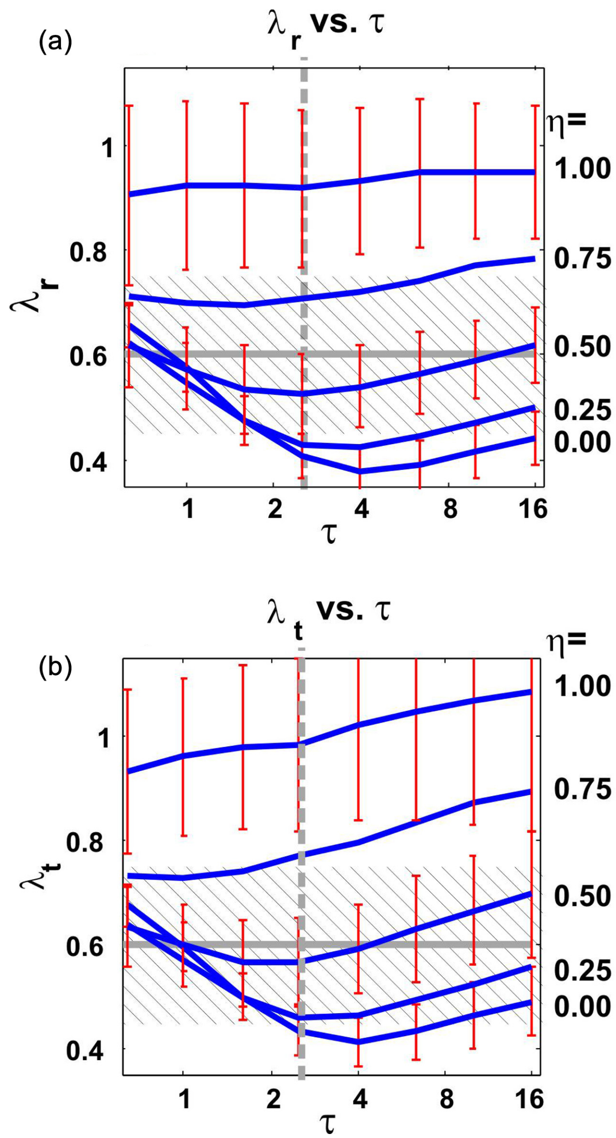

Figure 9. Relationships λ_r (τ) (a) and λ_t (τ) (b) for a number of η values. The hashed area indicates the approximate range of realistic λ values assumed to be equal to observational estimates of $\chi = -3\frac{d\log f_{c2}}{d\log M_0}$, see the Appendix for details. Grey solid line is the observed reference value (hypothetic average) taken as $\lambda = 0.60$. Dashed vertical line marks a tentative estimate of typical $\tau = 2.5$ reproduced from the previous picture.

range [0 1] was systematically studied for η. The effect of τ on λ_t (τ) and λ_r (τ) relationships is present but is not quite systematic; whereas the effect of variation of η is expressed. The increase of η results, at least at $\tau > 2$, in stable increase of λ_t and λ_r. Therefore, there are some chances to convert the values of λ derived from observations into at least rough estimate of η.

Figs 10 and 11 are given mostly for general understanding and are not used to derive any estimates. Fig. 10 shows the $w_{r100}(\tau)$ and $w_{t100}(\tau)$ relationships. The behaviour of $w_{r100}(\tau)$ is quite expectable. First, at a fixed distance $r_0 = 100$, front width $w(r_0)$ grows, in log–log scale, approximately linearly with increase of τ, reflecting increase of front width with increased degree of inhomogeneity. Second, it also systematically grows with increase of η. The cause of this tendency is less evident; its probable underpinning is that at the white noise case of $\eta = 0$, the effects of two adjacent heterogeneities can often be opposite and compensate one another,

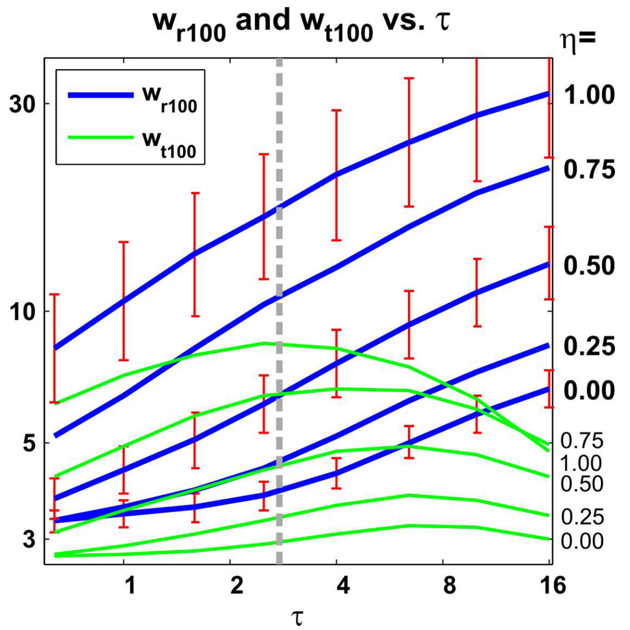

Figure 10. Relationships $w_{r100}(\tau)$ and $w_{t100}(\tau)$ for a number of η values. Note stable increase of w_{r100} both with τ and with η.

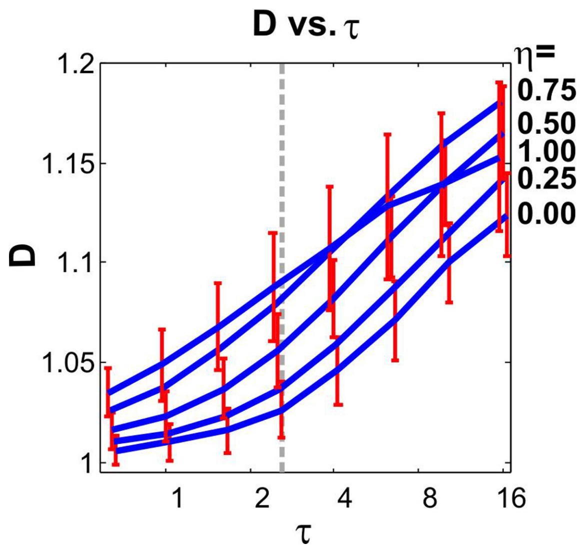

Figure 11. Fractal dimension D of irregular rupture front, plotted against τ, for a number of η values.

whereas at larger η (the case of expressed autocorrelation), many adjacent inhomogeneities affect a relevant segment of front in a coordinated way and therefore much more effectively. In the case of fixed propagation time $t_0 = 100$, the picture is different. The initial increase of w_{t100} (τ) is qualitatively similar to that of $w_{r100}(\tau)$, but it soon saturates and negative slope appears. This tendency reflects the fact that with increased fault heterogeneity, rupture velocity becomes relatively low; so at larger τ, w_{t100} cannot further follow the increase of τ, because w_{r100} is, intrinsically, proportional to propagation distance, and not to the time spent to reach this distance. On Fig. 11, $D(\tau)$ relationships are given. D increases with τ and, in the range $\eta = 0$–0.75, also with η. At $\eta = 1$, a tendency to saturation appears. Probably it develops further at $\eta > 1$ as suggested by less irregular shapes on Fig. 5(d) and especially Fig. 5(e).

With the relationships $m_r(\tau, \eta)$ and λ_r (τ, η) at hand, it is now possible to compare the calculated relationships with observational data, to be done in the next section.

5. COMPARING PARAMETERS OF SIMULATED FAULTS TO PROPERTIES OF REAL EARTHQUAKE SOURCES

In the current model, the style of fault evolution depends on the two parameters τ and η. Comparing observed parameters with those of simulated faults one may attempt to estimate the range of τ and η for real faults. These estimates will be very preliminary as they rely upon theoretical relationships of Figs 8 and 9 whose construction was based on simplifications and uncertain guesses. These are: unconstrained (near-circular in simple cases) rupture growth; self-similarity of Δt field; and exponential law for Δt distribution. Still, to find such estimates is at least a useful exercise; moreover, one can hope to obtain reasonable order-of-magnitude estimates.

Determination of reference values for properties of real faults is a separate problem, outside the line of this particular study; therefore it is moved to the Appendix. There, the following summary estimates are found through compilation: for normalized rupture velocity m (equated to m_r): the range 0.45–0.75, the reference value 0.6; for λ, equated here to λ_r: the range 0.45–0.75, the reference value 0.6 (the coincidence is accidental). It is assumed that $\lambda \approx \chi = \frac{d \log f_{c2}}{d \log f_{c1}}$. As must be clear from previous discussion, in order to estimate parameters τ and η of real faults one can try to use curves of Fig. 8 for τ, and those of Fig. 9 for η. On Fig. 8, point and interval estimates for m are shown at the ordinate axis. Similarly, On Fig. 9, point and interval estimates for λ_r are shown in similar way. Reference values are treated as point estimates. Using calculated trends of Figs 8 and 9 for calibration, from the observed values of m and λ_r, one can derive estimates of τ and η.

The chain of this derivation is presented in the Table 1. The initial acceptable range for η, of [0 1], is bounded: on the bottom—by the condition of not permitting blue noise Δt_{ij} field; on the top—by physically highly doubtful values $\lambda_r(\tau) > 1$ at $\eta > 1$, see Fig. 9. Bold values indicate accepted estimates. In selecting them, I believed that taking into account the range estimates simultaneously on both m and λ would result in unrealistically wide bounds. Summarizing, observational evidence combined with the theoretical curves of Figs 8 and 9 imply the following parameter estimates (rounded): point estimates: $\tau = 2.5$, $\eta = 0.6$; interval estimates: $\tau = 1$–6, $\eta = 0.25$–0.75.

6. GENERATING EXAMPLE SOURCE ACCELERATION SPECTRA

It is interesting to demonstrate operation of the developed concepts and to check their ability to produce verisimilar acceleration spectra. There are three specific features of HF part of source radiation: flat acceleration spectra ('ω^{-2}' property), two-corner spectral shape, and diminution of directivity at high frequencies. Among these, only the presence of the former two can and will be checked, because any effects of directivity are fully suppressed both by near-symmetric geometry of simulated front and by the selected position of the receiver.

To simulate source spectra (i.e. far-field body wave spectra), the procedure of G14 was used. I shall remind only its key points; a reader is addressed there for more details. The approach of G14 is based heavily on (Das & Kostrov 1983, 1986, 1988; Boatwright

Table 1. Steps of deriving estimates of model parameters from observational data.

Derivation step #	Input: Observed values	Input: estimates from previous steps	Fig. used[1]	Output
1	$m = 0.6$	$\eta_1 = [0\ 1]^2$	8	$\tau_1 = [2.1\ 3.8]$
2	$\lambda_r = 0.6$	τ_1	9	$\boldsymbol{\eta_2 = 0.62}^{3,4}$
3	$m = 0.6$	η_2	8	$\boldsymbol{\tau_2 = 2.5}^3$
4	$m = [0.45\ 0.75]$	η_2	8	$\boldsymbol{\tau_3 = [1.1\ 5.6]}^5$
5	$\lambda_r = [0.45\ 0.75]$	τ_2	9	$\boldsymbol{\eta_3 = [0.28\ 0.78]}^5$
6	$\lambda_r = [0.45\ 0.75]$	τ_3	9	$\eta_4 = [0\ 0.84]^{6,7}$
7	$m = [0.45\ 0.75]$	η_4	8	$\tau_4 = [1\ 8]^6$

[1]Number of the figure used for deriving the estimate.
[2]*A priori* bounds.
[3]The final point estimate.
[4]Employing the narrow range of the theoretical $m(\tau|\eta)$ curves of Fig. 8, the *interval* estimate for $\tau = \tau_1$ is converted here to the final *point* estimate of η, with accuracy ± 0.02.
[5]The final interval estimate. The narrower (preferred) version, anchored at the point estimate of another parameter.
[6]The final interval estimate. The wider (cautious) version, anchored at the interval estimate of another parameter.
[7]Formally, the values $\eta < 0$ are also possible; these were excluded as improbable.

1988; Gusev 1989). The initial (not realistic) model is one of an infinite zero-strength fault, with a strong patch or asperity that occupies a bounded area Σ_a on it, loaded by shear load. The term 'asperity' is used here, following Boatwright (1988), in a loose sense; the patch Σ_a can be relatively strong or weak; the only requirement is finite strength. Rupture front nucleates at some point of Σ_a, and then sweeps over it; this causes successive failure of fault elements. Failure of an element is instant in terms of stress drop (not in terms of slip!). This failure generates body waves in each half-space, and also fault-guided wave train, mostly of Rayleigh waves. For the characteristic case of *SH* wave, the displacement and velocity from a fault element dS at a far-field receiver at a point $\mathbf{x}' = \{x', y', z'\}$ and time t can be written as

$$du^{SH,\infty}(\mathbf{x}\prime, t) = A\tau'(\xi)H(t - (R - \xi\cdot\gamma)/c_S - t_{fr}(\xi))dS; \quad A = \frac{\Re_F^{SH}}{4\pi\rho c_S^2 R} \tag{3a}$$

$$d\,\dot{u}^{SH,\infty}(\mathbf{x}\prime, t) = A\tau'(\xi)\delta(t - (R - \xi\cdot\gamma)/c_S - t_{fr}(\xi))dS \tag{3b}$$

where $\xi = \{x, y, 0\}$ is location of dS, the hypocentre is at $\xi = 0$; $\tau'(\xi)$ is local dynamic stress drop on dS; $R = |\,\mathbf{x}'\,|$; $\boldsymbol{\gamma} = \mathbf{x}'/R$; ρ is density; c_S is *S*-wave velocity; $t_{fr}(\xi)$ is the time of arrival of rupture front to ξ; $\Re_F^{SH}$ is the radiation pattern of *SH* waves radiated by a point *force*; $H(\cdot)$ is unit step and $\delta(\cdot)$ is delta-function. Thus, failure at dS produces elementary step in far-field displacement. Integration of (3a) over Σ_a produces the initial variant of source time function. Note that (1) far-field force equivalent for this model is single-dipole, and (2) its seismic moment M_0 is integral of a sum of step functions, therefore it equals infinity.

The next step to more realism is to account for limited size of a free-slipping area, introducing a boundary which exists somewhere around Σ_a on a real geological fault. Denote the area enclosed by the boundary and containing Σ_a as Σ. Outside Σ entire fault is now welded. This causes dying out of fault-guided waves (which include running dislocation step) at some distance from the asperity Σ_a. This stopping of fault-guided waves converts step function (3a) into an elementary unipolar pulse of finite duration, with abrupt leading and, (typically) gradual trailing edges; let its shape be described by $G_0(t, \xi)$. It is at this moment that the second dipole appears. It precisely compensates the initial one in terms of torque; this guarantees symmetry of the resulting seismic moment tensor (Aki & Richards 2002, sect 3.2). Far-field wave displacement time function is now pulse-like and provides finite seismic moment.

And the final step (Boatwright 1988) is to assume that the entire area Σ is completely covered by 'asperities' whose contributions into the far-field waveform are additive. To obtain approximate estimates, the duration and shape of the $G_0(t, \xi)$ pulse was assumed identical for all radiating spots on the fault: $G_0(t, \xi) = G(t)$. This element of the G14 procedure was followed here.

The pulse shape $G(t)$, was selected following Boatwright (1988), as

$$G(t) = \begin{cases} H(t) - 0.5(1 + \cos\pi t/T_B; & t < T_B \\ 0 & t > T_B \end{cases} \tag{4}$$

where duration parameter T_B was selected following the assumption that it is directly defined by the front width: $T_B = 1.67T_r$ where T_r is rise time: $T_r = w_{fr}/m_r$. The rupture front both in the numeric model G14 and here consists of a set of cells; only here they are components of the fault model and not mere finite elements as in G14. Each cell generates a spike timed at the arrival of front to it. The sequence of spikes arrived to receiver was convolved with the $G(t)$ pulse. This convolution corresponds to certain filter in frequency domain. It is just this filter that forms second spectral corner, located at $f_{c2} \approx 0.5/T_r$.

An important component of G14 was setting stress drop field $\tau'(\xi) = \tau'_{ij}$. It was simulated as realization of self-similar random field with amplitude spectrum of the $k^{-\alpha}$ kind, with the particular value of α set to 1.0. It was shown in G14 that the described procedure results in spectra and traces, which satisfy acceptably the three requirements listed above. In the current simulation, the stress field ($\tau'(\xi) = \tau'_{ij}$) model of G14 was used again. Generally speaking, instead of generating Δt_{ij} and τ'_{ij} as independent random fields one might introduce correlation between them, in the manner of for example Schmedes *et al.* (2012). Unfortunately, no good way is seen to predict the kind of such correlation. For heterogeneity of the 'barrier' kind, high (dynamic) stress drop is related to high local strength, low local v_r and large Δt_{ij}. Oppositely with heterogeneity of the 'asperity' kind, high local stress drop is related to a highly loaded spot which may break with a minimal delay. As in reality both modes probably combine, the independence of Δt_{ij} and τ'_{ij} looks as a reasonable initial choice.

To perform simulation, one has to define elementary contribution from a unit cell. As seen from (3b), for far-field velocity time function this contribution is delta-like for infinitesimally small fault element, and therefore can be taken as one-sided pulse for a finite cell of the model. The shape of this 'unit' pulse must be selected sufficiently smooth to create no spectral distortions. I used pulse shape function

$$F_c(t') = t'^2 \exp(t'), \text{ with } t' = t/2T_{c3} \tag{5}$$

where $2T_{c3}$ is the characteristic cell time, and T_{c3} is the halfwidth (onset to centroid time) of unit pulse. This function is selected in order to provide f^{-3} falloff of acceleration spectrum at HF. The value of T_{c3} is related to the time interval that the rupture needs to cross a cell. Therefore, it was assumed that T_{c3} depends linearly on τ, and the following formula was found by try and error:

$$T_{c3} = 1.55 + 0.125t. \tag{6}$$

The value of T_{c3} defines the location of the upper cut-off of acceleration spectrum, that is source-controlled f_{max}, or f_{c3}. In entire simulation of signals and spectra, the time step was set to 0.25; this choice occurred to be sufficient to sidestep any significant artefacts. The pulse (5) was used in convolution in the same manner as the pulse (4).

In simulation of earthquake rupture, one should be accurate with effects of rupture termination: when it is described inadequately, artefacts in the form of unrealistically sharp stopping phases may appear, distorting accelerograms and their spectra. In G14, the rupture run over a rectangular area, and nucleation point was located near one of its corners; thus stopping of propagation at the contour of the area was rather stretched out in time. For this reason, without any special measures, no significant contamination from stopping phases arose. In the present case, when entire rupture front is stopped simultaneously, and the receiver is located on fault normal, the displacement time history at the receiver shows abrupt, jump-like, termination. Corresponding powerful spikes appear on velocity and acceleration traces, and spectra are severely distorted. For this reason, in order to generate more verisimilar time histories and spectra, simulated seismograms are artificially tapered over their later part.

Three particular pairs of parameters (τ, η) were chosen to produce different intervals between f_{c1} and f_{c2}, and three corresponding series of accelerograms and spectra were generated. Each series included 20 Monte Carlo runs (Fig. 12). One can see acceleration spectra with two corners and a considerable range of plateau-like behaviour. Originally, simulated seismic moments, M_0, varied somewhat from one MC run to another because random realizations of local stress drop (and implicitly of slip) were non-identical. To compensate related scatter of no deep meaning, all spectra were reduced to the common M_0 (average of the original series). To make visible different relative levels of HF spectral plateau, A_{HF}, spectra were once more normalized, now jointly, setting their average level to unity at f_{c1}. All simulated space–time histories were played on the same 400 × 400 grid; but time history durations, and with them f_{c1} values, varied somewhat depending on the average rupture velocity (which is defined mostly by τ, Fig. 8). The (relative) position of the second corner varies significantly, depending on the width of rupture front, as expected. The case of Fig. 12(a) is one of a wide front and thus of low f_{c2}/f_{c1} ratio, with plateau of acceleration spectrum well discernible and relatively low. The cases of Figs 12(b) and (c) are of more and more narrow front, with increasingly higher level of the plateau of acceleration spectrum. Unexpectedly, the slope of the plateau is not completely stable: slopes vary systematically from negative to positive values, within the range ±0.2. Still, around the preferable values ($\tau = 2.5$, $\eta = 0.6$) the slope is quite close to zero,

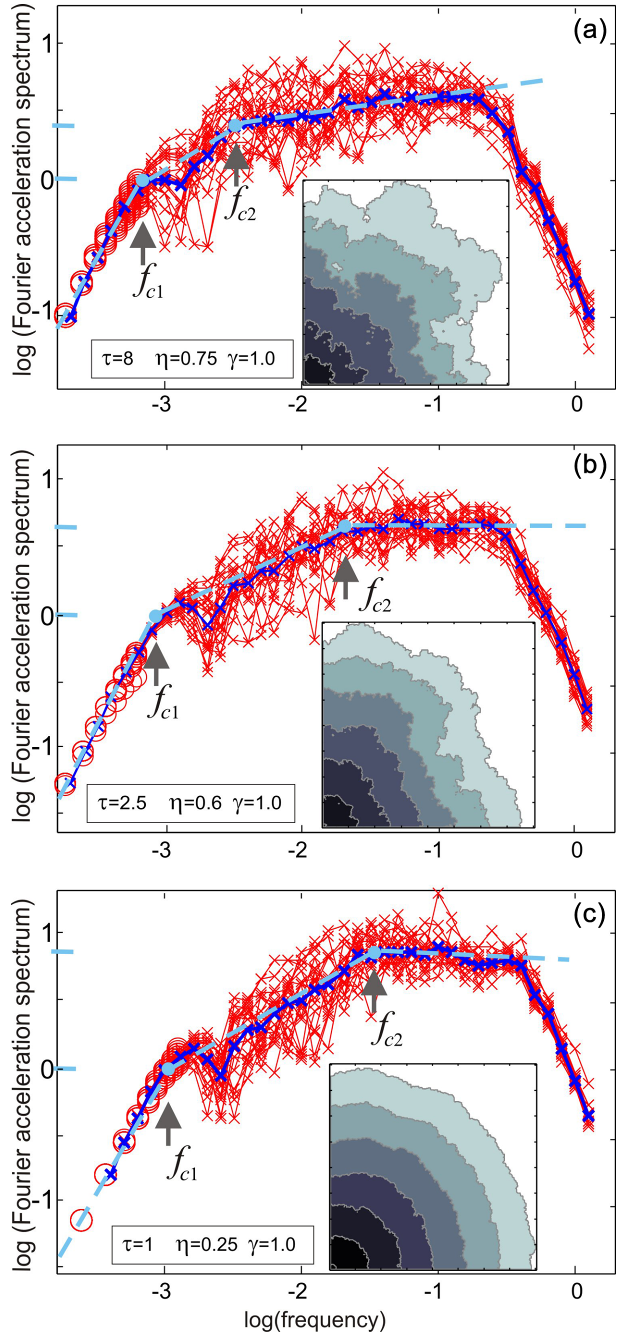

Figure 12. (a) Average (blue) of 20 simulated source acceleration spectra (red) for the case $\eta = 0.75$, $\tau = 8$. Lines with crosses are for spectra averaged over log-uniformly located bands. Red circles are points of unsmoothed spectrum. Cyan dotted line depicts idealized two-corner spectrum. Grey arrows and cyan dots mark corner frequencies; their ratio $f_{c2}/f_{c1} = 5$. Cyan dashes at the ordinate axis denote spectral levels at corner positions. Insert shows example front history over the 400 × 400 simulation quadrant used. Ordinate scale, uncalibrated originally, is shifted vertically to set the spectral level at f_{c1} to unity. For the explanation of the upper spectral cut-off see text. (b) Similar picture for the case $\eta = 0.6$, $\tau = 2.5$; $f_{c2}/f_{c1} = 22$. (c) Similar picture for the case $\eta = 0.25$, $\tau = 1$; $f_{c2}/f_{c1} = 30$.

in a good match with the 'ω^{-2}' concept. To conclude, within the performed simulation test the expected appearance of spectrum was successfully realized: one sees a two-corner spectrum with acceleration spectral plateau.

7. DISCUSSION

Departing from the typical ranges of observed parameters $m_r = 0.45$–0.75, $\lambda = 0.45$–0.75, this research resulted in tentative ranges of model parameters: mean additional delay per cell $\tau = 1$–6, the exponent of 2-D amplitude spectrum of delay field $\eta = 0.25$–0.75. As a point estimate, one may accept $\tau = 2.5$, $\eta = 0.6$. It is interesting to juxtapose the obtained estimates with parameters of real faults. The proposed range of η can be compared to other spectral exponents of fault surface. As delay field in the present model may represent strengths of cells, an appropriate candidate for comparison is local stress drop, which may reflect local strength. Mai & Beroza (2002) found the typical value for amplitude spectral exponent for slip to be 1.75, this suggests the exponent for stress drop field $\alpha = 0.75$. However, Lavallée *et al.* (2006) believe that high-wavenumber components of slip spectrum may be artificially suppressed during inversion procedures. Their preferred estimates for α are in the range (-0.15)-(+ 0.35), with the average value around zero. It was also proposed to associate local fault strength with the local slope of fault geometrical profile (Main 1988). Candela *et al.* (2012) found amplitude spectrum of fault profile to behave as $k^{-(0.6-0.8)}$. For a hypothetic fresh rupture with such a profile, Main's logic gives 'blue' strength spectrum ($k^{+(0.2-0.4)}$), predicting anticorrelation of strength between adjacent spots; but the applicability of this approach is disputable. Taking into account these not quite consistent pieces of information, we can treat the obtained range $\eta = 0.25$–0.75 as quite acceptable.

As regards τ, its point estimate of 2.5 may look strange. Indeed, at mean velocity of $m = 0.6$, mean delay per unit distance, that is per cell size, is $\tau^* = m^{-1} = 1.67$. At the same time, full average delay per cell is much larger: $\langle \Delta t_{ij}^{(f)} \rangle = \langle \Delta t_o \rangle + \langle \Delta t_{ij} \rangle = 1.25 + \tau = 1.25 + 2.5 = 3.75$. This contradiction is apparent however as it tacitly assumes that the failure process develops along a single chain of cells. In fact, however, for a certain cell of a front line, among its eight neighbour cells, about four of them have already failed before, and any of the four can 'ignite' it. At the simplest assumption that all the four themselves were 'ignited' simultaneously, actual effective additional delay per cell will be on the order of the smallest value among four independent exponentially distributed random numbers, equal on the average to $\tau'' = 0.25\tau$, or 0.63. Adding mean propagation delay of 1.25 gives 1.88, in an unexpectedly good match to the above-discussed value $\tau^* = 1.67$. This match should not be taken too seriously: there are other participating factors. Firstly, rupture front can go around strong spots of the general strength relief rather effectively; and this Fermat-style 'optimization' increases observed velocity as compared to the rough estimate. There is another factor, whose effect is of opposite sign : the propagating rupture spends additional time, as compared to straight-line propagation, because of random curved path of the 'ignition signal' (Fig. 2). It is difficult to estimate contributions of the last two effects into final observed velocity; still they look as secondary. It is possible to conclude that the obtained estimate of τ shows no striking misfit when compared to the empirical average/typical value of m.

Evidently, some characteristic properties of real earthquake sources are not described within the limits of the performed simulation. First of all, it is elongated fault geometry; also it is often unilateral propagation mode. Within the present general approach, this behaviour can be easily simulated quite traditionally, adding suitable artificial external borders, and positioning the nucleation point asymmetrically within them. This was done in G14 where the borders were impenetrable (of infinite strength). Such artificial barriers are somewhat doubtful tectonophysically, and may also produce unwanted stopping phases. Another way to stop rupture (or to switch off radiation) might be to taper stress drop field along the periphery of simulation area. Both these approaches look acceptable for future study, though somewhat artificial.

As regards unilateral propagation mode in particular, it was found by try and error that asymmetric propagation can be simulated within the developed approach (see Fig. 3c). It was found however, that to generate unilateral ruptures, one needs to significantly enhance low-wavenumber part of delay spectrum. To achieve this, one can either use unrealistic η values around or above 2.0, or to admix low-wavenumber term to the main self-similar delay field. Both ways look unattractive. Also, the problem of fully consistent stopping of a rupture remains unresolved in this approach. Generally, causes of unilateral elongated ruptures seem to be an open question.

It was found in G14 that at fixed values of fault size L, seismic moment M_0 and fault-average stress drop $\langle \Delta\sigma \rangle$, A_{HF} and correspondingly the value of 'stress parameter' are determined by the w_{fr}/L ratio. The present results (Fig. 12) permit to extend this chain of relationships and to formulate the following statement: at given values of L, $M_{0,} \langle \Delta\sigma \rangle$ and of spectral exponent of fault heterogeneity, η, both the A_{HF} and the 'stress parameter' are determined at least partly by the value of mean delay parameter τ, which operates through the intermediate w_{fr} parameter. Generally, the larger is τ, the larger is w, the lower is the f_{c2}/f_{c1} ratio and the lower is A_{HF}. This concordant behaviour of f_{c2} and A_{HF} is well seen on Fig. 12; the effect of some variations of η is secondary. Therefore, the results of simulation by the kinematic cellular model may improve understanding of physical factors that affect strong ground motion amplitudes.

An important absent point is the direct comparison of w values to observations (e.g. to slip pulse width). To do this, one needs at first to pass from dimensionless values of time and distance used here, to natural scales. To do this one needs observational estimates of unit cell size. As noted in Introduction, its order of magnitude is, roughly, 100–300 m, but establishing it more accurately is a point of a separate study.

Another point for future study is the effects of various probability laws for local values of delay field. The absence of such analysis is the main cause why the present study should be qualified, rather, as a demonstration of concept. Confident estimates of parameters τ and η can be obtained only when a proper probability law is assumed; thus, the estimates obtained above should be treated as tentative. Some less significant generalizations of the present approach are also possible, for example permitting negative values for Δt_{ij}, and thus allowing 'lakes' of front line. However, first experiments along his line did not indicate any qualitative changes of behaviour of the model.

8. CONCLUSION

A continuous-time cellular model is designed, aimed at description of the evolution of random rupture front during formation of earthquake source. The particular version of the model is developed, controlled by two parameters: mean additional front delay per cell, τ; and the exponent η of power-law power spectrum of assumedly self-similar 2-D random delay field.

A set of parameters of rupture evolution is introduced and a technique for their estimation is proposed. Among them, the two are found which can be compared to parameters of real earthquake ruptures. These are: normalized front velocity m (Mach number), and the exponent λ which describes how fast the rms width of random front increases in the process of front propagation.

By Monte Carlo experiments, a variant of relationships $m(\tau, \eta)$ and $\lambda(\tau, \eta)$ is determined. On this basis, and using observational data on m and λ, tentative estimates of τ and η for real faults are derived.

Numerical experiments were performed in which the simulated rupture fronts were combined with a realistic model of local stress drop field over a fault surface; radiated far field body wave acceleration signals from such sources were found and converted to spectra. These spectra bear two characteristic properties of observed source acceleration spectra: two distinctive spectral corners, and a plateau above the second corner frequency.

Despite being kinematic, the developed model provides some insight into the physical mechanisms which control strong ground motion amplitudes; it therefore may occur useful for eventual prediction of realistic strong motion and for estimation of its variability.

ACKNOWLEDGEMENTS

The study was partly supported by the Russian Ministry of Education and Science under the grant 14.W03.31.003. The author is grateful to A. Herrero and to anonymous reviewer for useful criticism and valuable suggestions which helped to improve the manuscript.

REFERENCES

Aguirre, J. & Irikura, K., 2007. Source characterization of Mexican subduction earthquakes from acceleration source spectra for the prediction of strong ground motions, *Bull. seism. Soc. Am.,* **97,** 1960–1969.

Aki, K. & Jin, A., 2000. Seismic monitoring and modeling of earthquake processes for prediction, in *Proceedings of the 2nd ACES Workshop,* pp. 121–127, Tokyo and Hakone, Japan.

Aki, K. & Richards, P.G., 2002. *Quantitative seismology,* 2nd ed., University Science Books.

Andrews, D.J., 1976. Rupture velocity of plane strain shear cracks, *J. geophys. Res.,* **81**(32), 5679–5687.

Andrews, D.J., 1980. A stochastic fault model. 1. Static Case, *J. geophys. Res.,* **78,** 3867–3877.

Archuleta, R.J., 1984. A faulting model for the 1979 Imperial Valley earthquake, *J. geophys. Res.,* **89,** 559–4585.

Archuleta, R.J. & Ji, C., 2016. Moment rate scaling for earthquakes 3.3 $\leq$ M $\leq$ 5.3 with implications for stress drop, *Geophys. Res. Lett.,* **43,** doi:10.1002/2016GL071433.

Atkinson, G.M., 1993. Earthquake source spectra in Eastern North America, *Bull. seism. Soc. Am.,* **83,** 1778–1798.

Atkinson, G.M. & Boore, D.M., 1998. Evaluation of models for earthquake source spectra in eastern North America, *Bull. Seismol. Soc. Amer.,* **88**(4), 917–934.

Ben-Zion, Y. & Rice, J.R., 1993, Earthquake failure sequences along a cellular fault zone in a three-dimensional elastic solid containing asperity and nonasperity regions, *J. geophys. Res.,* **98,** 14 109–114 131.

Beresnev, I. & Atkinson, G., 2002. Source parameters of earthquakes in eastern and western North America based on finite-fault modeling, *Bull. seism. Soc. Am.,* **92,** 695–710

Bernard, P. & Herrero, A., 1994. Slip heterogeneity, body-wave spectra, and directivity of earthquake ruptures, *Ann. Geofis.,* **XXXVII**(6), 1679–1690.

Blaser, L., Krüger, F., Ohrnberger, M. & Scherbaum, F., 2010. Scaling relations of earthquake source parameter estimates with special focus on subduction environment, *Bull. seism. Soc. Am.,* **100,** 2914–2926.

Boatwright, J., 1988. The seismic radiation from composite models of faulting, *Bull. seism. Soc. Am.,* **78**(2), 489–508

Boatwright, J. & Quin, H., 1986. The seismic radiation from a 3D dynamic model of a complex rupture process. *Part I: confined ruptures,* AGU Geophysical Monograph Series, Vol. **37,** pp. 97–109.

Bonamy, D., 2009. Intermittency and roughening in the failure of brittle heterogeneous materials, *J. Phys. D: Appl. Phys.,* **42**(21), 214014.

Boore, D.M. & Joyner, W.B., 1978. The influence of rupture incoherence on seismic directivity, *Bull. seism. Soc. Am.,* **68**(2), 283–300.

Burridge, R. & Knopoff, L., 1967. Model and theoretical seismicity, *Bull. seism. Soc. Am.,* **57**(3), 341–371.

Candela, T., Renard, F., Klinger, Y., Mair, K., Schmittbuhl, J. & Brodsky, E.E., 2012. Roughness of fault surfaces over nine decades of length scales, *J. geophys. Res.,* **117,** B08409, doi:10.1029/2011JB009041.

Chouet, B., Aki, K. & Tsujiura, M., 1978. Regional variation of the scaling law of earthquake source spectra, *Bull. seism. Soc. Am.,* **68,** 49–79.

Crempien, J.G. & Archuleta, R.J., 2015. UCSB method for simulation of broadband ground motion from kinematic earthquake sources, *Seismol. Res. Lett.,* **86**(1), 61–67.

Das, S. & Kostrov, B.V., 1983. Breaking of a single asperity: rupture process and seismic radiation, *J. geophys. Res.,* **88**(B5), 4277–4288.

Das, S. & Kostrov, B.V., 1986. Fracture of a single asperity on a finite fault: a model for weak earthquakes? in *Earthquake Source Mechanics,* Vol. **37,** pp. 91–96, AGU Geophysical Monograph Series.

Das, S. & Kostrov, B.V., 1988. An investigation of the complexity of the earthquake source time function using dynamic faulting models, *J. geophys. Res.,* **93**(B7), 8035–8050

Day, S., 1982. Three dimensional simulation of spontaneous rupture: the effect of non-uniform pre-stress, *Bull. seism. Soc. Am.,* **72,** 1881–1902.

Day, S.M., Gonzalez, S.H., Anooshehpoor, R. & Brune, J.N., 2008. Scale-model and numerical simulations of near-fault seismic directivity, *Bull. seism. Soc. Am.,* **98**(3), 1186–1206.

Denolle, M.A. & Shearer, P.M., 2016. New perspectives on self-similarity for shallow thrust earthquakes, *J. geophys. Res.,* **121**(9), 6533–6565.

Dunham, E.M., Belanger, D., Cong, L. & Kozdon, J.E., 2011. Earthquake ruptures with strongly rate-weakening friction and off-fault plasticity. Part 2: nonplanar faults, *Bull. seism. Soc. Am.,* **101,** 2308–2322.

Duputel, Z., Tsai, V.C., Rivera, L. & Kanamori, H., 2013. Using centroid time-delays to characterize source durations and identify earthquakes with unique characteristics, *Earth planet. Sci. Lett.,* **374,** 92–100.

Feller, W., 1957. *An Introduction to Probability Theory and Its Applications,* Vol. **1,** Ch. XIV, J. Wiley & Sons.

Fineberg, J. & Marder, M., 1999. Instability in dynamic fracture, *Phys Rep.,* **313,** 1–108.

Geller, R.J., 1976. Scaling relations for earthquake source parameters and magnitudes, *Bull. seism. Soc. Am.,* **66,** 1501–1523.

Goda, K, Mai, P.M., Yasuda, T. & Mori, N., 2014. Sensitivity of tsunami wave profiles and inundation simulations to earthquake slip and fault geometry for the 2011 Tohoku earthquake, *Earth, Planets Space,* **66,** 105.

Gouyet, J.-F., 1996. *Physics and Fractal Structures,* Chapter 4: Growth Models. Springer.

Guatteri, M., Mai, P.M. & Beroza, G.C., 2004. A pseudo-dynamic approximation to dynamic rupture models for strong ground motion prediction, *Bull. seism. Soc. Am.,* **94,** 2051–2063.

Gusev, A.A., 1983. Descriptive stochastic model of earthquake source radiation and its application to an estimation of short-period strong motion, *Geophys. J. R. astr. Soc.,* **74,** 787–808

Gusev, A.A., 1989. Multiasperity fault model and the nature of short-period subsources, *Pure Appl. Geophys.,* **130,** 635–660.

Gusev, A.A., 2011. Broadband kinematic stochastic simulation of an earthquake source: a refined procedure for application in seismic hazard studies, *Pure appl. Geophys.,* **168,** 155–200.

Gusev, A.A., 2013. High-frequency radiation from an earthquake fault: a review and a hypothesis of fractal rupture front geometry, *Pure appl. Geophys.,* **170,** 65–93.

Gusev, A.A. & Guseva, E.M., 2016. Source spectra of Near Kamchatka Earthquakes: recovering them from S-wave spectra, and determination of scaling for three corner frequencies, *Pure appl. Geophys.,* **173,** 1539–1557.

Gusev, A.A. & Pavlov, V.M., 1991. Deconvolution of squared velocity waveform as applied to study of noncoherent short-period radiator in earthquake source, *Pure appl. Geophys.,* **136,** 235–244

Gusev, A.A. & Pavlov, V.M., 2009. Broadband simulation of earthquake ground motion by a spectrum matching, multiple-pulse technique, *Earthq. Spectra,* **25**(2), 257–276.

Gusev, A.A., 2014. Doubly stochastic earthquake source model: "omega-square" spectrum and low high-frequency directivity revealed by numerical experiments, *Pure appl. Geophys.,* **171,** 2581–2599.

Halldorsson, B. & Papageorgiou, A.S., 2005. Calibration of the specific barrier model to earthquakes of different tectonic regions, *Bull. seism. Soc. Am.,* **95,**1276–1300.

Halpin-Healy, T. & Zhang, Y.-Ch., 1995. Kinetic roughening phenomena, stochastic growth, directed polymers and all that, *Physics Reports,* **254,** 215–414

Hanks, T.C., 1979. b-values and $\omega-\gamma$ seismic source models: implications for tectonic stress variations along active crustal fault zones and the estimation of high-frequency strong ground motion, *J. geophys. Res.,* **84,** 2235–2242.

Heaton, T.H., 1990. Evidence for and implications of self-healing pulses of slip in earthquake rupture, *Phys. Earth planet. Inter.,* **64,** 1–20.

Herrero, A. & Bernard, P., 1994. A kinematic self-similar rupture process for earthquakes, *Bull. seism. Soc. Am.,* **84,** 1216–1228.

Houston, H., 2001. Influence of depth, focal mechanism, and tectonic setting on the shape and duration of earthquake source time functions. Journal of Geophysical Research, *Solid Earth,* **106**(B6), 11137–11150.

Israel, M. & Nur, A., 1979. A complete solution of a one-dimensional propagating fault with nonuniform stress and strength, *J. geophys. Res.,* **84**(B5), 2223–2234.

Joyner, W.B., 1991. Directivity for nonuniform ruptures, *Bull. seism. Soc. Am.,* **81**(4), 1391–1395.

Kaneko, Y. & Shearer, P.M., 2014. Seismic source spectra and estimated stress drop derived from cohesive-zone models of circular subshear rupture, *Geophys. J. Int.,* **197**(2), 1002–1015.

Kostrov, B.V., 1975. *Mechanics of the Source of a Tectonic Earthquake,* Nauka.

Koyama, J. & Shimada, N., 1985. Physical basis of earthquake magnitudes: an extreme value of seismic amplitudes from incoherent fracture of random fault patches, *Phys. Earth planet. Inter.,* **40,** 301–308.

Lavallée, D., Liu, P.-Ch. & Archuleta, R.J., 2006. Stochastic model of heterogeneity in earthquake slip spatial distributions, *Geophys. J. Int.,* **165,** 622–640.

Leonard, M., 2010. Earthquake fault scaling: Self-consistent relating of rupture length, width, average displacement, and moment release, *Bull. seism. Soc. Am.,* **100**(5A), 1971–1988.

Lomnitz-Adler, J. & Lund, F., 1992. The generation of quasi-dynamical accelerograms from large and complex seismic fractures, *Bull. seism. Soc. Am.,* **82**(1), 61–80.

Madariaga, R., 1977. High-frequency radiation from crack (stress drop) models of earthquake faulting, *Geophys. J. Int.,* **51,** 625–651.

Madariaga, R., 1983. High frequency radiation from dynamic earthquake fault models, *Ann. Geophys.,* **1,** 17.

Madariaga, R. & Olsen, K.B., 2002. Earthquake dynamics, *Int. Geophys. Ser.,* **81** (A), 175–194.

Main, I., 1988. Prediction of failure times in the Earth for a time-varying stress, *Geophys. J.,* **92,** 455–464.

Mai, P.M. & Beroza, G.C., 2002. A spatial random field model to characterize complexity in earthquake slip, *J. geophys. Res.,* **107**(B11), 2308.

Mai, P.M. & Thingbaijam, K.K.S., 2014. SRCMOD: an online database of finite-fault rupture models, *Seismol. Res. Lett.,* **85**(6), 1348–1357.

Mandelbrot, B.B., 1982. *The Fractal Geometry of Nature,* pp 468, W.H. Freeman.

Manighetti, I., Campillo, M., Sammis, C., Mai, P.M. & King, G., 2005. Evidence for self-similar, triangular slip distributions on earthquakes: implications for earthquake and fault mechanics, *J. geophys. Res.,* **110**(B5), doi:10.1029/2004JB003174.

Morozov, N.F. & Petrov, Y.V., 2002. Quantum nature and dual character of fracture dynamics in solids, *Doklady Physics,* **47,** 85–88

Novozhilov, V.V., 1969. On a necessary and sufficient criterion for brittle strength, *J. Appl. Math. Mech.-USSR,* **33,** 212–222.

Papageorgiou, A.S. & Aki, K., 1983. A specific barrier model for the quantitative description of inhomogeneous faulting and the prediction of strong ground motion. I. Description of the model, *Bull. seism. Soc. Am.,* **73,**693–722.

Papageorgiou, A.S. & Aki, K., 1985. Scaling law of far-field spectra based on observed parameters of the specific barrier model, *Pure Appl. Geoph.,* **123,** 353–374.

Perrin, G. & Rice, J.R., 1994. Disordering of a dynamic planar crack front in a model elastic medium of randomly variable toughness, *J. Mech. Phys. Solids,* **42,** 1047–1064,

Rice, J.R., 1980. The mechanics of earthquake rupture, in *Physics of Earth's Interior (Proc.Int'l School of Physics "Enrico Fermi", course 78, 1979),* pp. 194, eds Dzievonski, A.M. & Boschi, E., Italian Physical Society/North Holland.

Rydelek, P.A. & Sacks, I.S., 1996. Earthquake slip rise time and rupture propagation: Numerical results of the quantum earthquake model, *Bull. seism. Soc. Am.,* **86,** 567–574.

Sacks, I.S & Rydelek, P.A., 1995. Earthquake "Quanta" as an explanation for observed magnitudes and stress drops, *Bull. seism. Soc. Am.,* **85,** 808–813.

Schmedes, J., Archuleta, R.J. & Lavallée, D., 2012. A kinematic rupture model generator incorporating spatial interdependency of earthquake source parameters, *Geophys. J. Int.,* **192**(3), 1116–1131.

Scholz, C.H. & Lawler, T.M., 2004. Slip tapers at the tips of faults and earthquake ruptures, *Geophys. Res. Lett.,* **31**(21), doi:10.1029/2004GL021030.

Seekins, L.C. & Boatwright, J., 2010. Rupture directivity of moderate earthquakes in northern California, *Bull. seism. Soc. Am.,* **100,** 1107–1119.

Shearer, P.M., 1999. *Introduction to Seismology,* Cambridge Univ. Press.

Somerville, P. *et al.*, 1999. Characterizing crustal earthquake slip models for the prediction of strong motion, *Seism. Res. Lett.,* **70,** 59–80.

Somerville, P.G., Smith, N.F., Graves, R.W. & Abrahamson, N.A., 1997. Modification of empirical strong ground motion attenuation relations to include the amplitude and duration effects of rupture directivity, *Seism. Res. Lett.,* **68,** 199–222.

Song, S.G., Dalguer, L.A. & Mai, P.M., 2014. Pseudo-dynamic source modelling with 1-point and 2-point statistics of earthquake source parameters, *Geophys. J. Int.,* **196**(3), 1770–1786.

Spudich, P. & Cranswick, E., 1984. Direct observation of rupture propagation during the 1979 Imperial Valley earthquake using a short baseline accelerometer array, *Bull. seism. Soc. Am.,* **74**(6), 2083–2114.

Stein, S. & Wysession, M., 2003. *An Introduction to Seismology, Earthquakes and Earth Structure,* Blackwell.

Tanioka, Y. & Ruff, L.J., 1997. Source time functions, *Seismol. Res. Lett.,* **68,** 386–400.

Tsai, C.-C.P., 1997. Ground motion modeling for seismic hazard analysis in the near-source regime: an asperity model, *Pure appl. Geophys,* **149,** 265–297.

Vallée, M., 2013. Source time function properties indicate a strain drop independent of earthquake depth and magnitude, *Nat. Commun.,* **4,** 2606.

Wang, Y. & Day, S.M., 2017. Seismic source spectral properties of crack-like and pulse-like modes of dynamic rupture, *J. Geophys. Res. Solid Earth,* **122,** 6657–6684, doi:10.1002/2017JB014454.

Wells, D.L. & Coppersmith, K.J., 1994. New empirical relationships among magnitude, rupture length, rupture width, rupture area, and surface displacement, *Bull. seism. Soc. Am.,* **84**(4), 974–1002.

Wilkins, S.J. & Schultz, R.A., 2005. 3D cohesive end-zone model for source scaling of strikeslip interplate earthquakes, *Bull. seism. Soc. Am.,* **95,** 2232–2258.

Ye, L., Lay, T., Kanamori, H. & Rivera, L., 2016. Rupture characteristics of major and great ($M_w \geq 7.0$) megathrust earthquakes from 1990 to 2015: 1. Source parameter scaling relationships, *J. geophys. Res.,* **121**(2), 826–844.

APPENDIX: COMPILING EMPIRICAL ESTIMATES FOR THE VALUES OF FAULT PARAMETERS

To make meaningful comparison with the results of simulation I need observational estimates of scaled rupture velocity, m, and of exponent of log w versus log L relationship, λ.

Rupture velocity

In this subsection data will be compiled on $m = v_r/c_S$. Early estimates of v_r were compiled by Geller (1976) who converted them to m. His average, $m = 0.72 \approx 0.7$ over 23 cases was widely accepted. Recently, estimates of v_r for 114 $M_w \geq 7$ subduction earthquakes were obtained by Ye *et al*. (2016) who performed mass inversion of rupture evolution for each event. Their reference point estimate is $v_r = 2.5$ km s^{-1}, and interval estimate is 2.0–3.0 km s^{-1}. For subduction events, there is no well-established estimate of c_S as this interface is to a large degree bimaterial. I chose $c_S = 4$ km s^{-1} and got: average $m = 0.625$, and the range 0.5 to 0.75. For 47 $M_w = 3.5$–5.4 earthquakes analysed using regional Northern California data, Seekins & Boatwright (2010) obtained average m around 0.8 and about 10 per cent data with $v_r > 1$ (intersonic). The difference with large subduction events may result from simpler, typically unit-segment $M_w = 3.5$–5.4 sources as compared to often multisegment ruptures of large events.

Independent estimates of m can be derived combining rupture duration d and fault length L data. One can estimate v_r as $\theta L/d$ where θ is the average degree of unilaterality of ruptures; its preferred value must be assumed. I set it to 0.875 which is the average between the purely unilateral case of $\theta = 1$ and the case of uniform random distribution of hypocentre along length, which gives $\theta = 0.75$. Estimates will be further discussed based on empirical regressions of d and L for shallow earthquakes picked at $M_w = 7$. An alternative to d proper is using somewhat more stable temporal centroid d_c that can be equated to 0.5d. Regression of Duputel *et al.* (2013) gives $d_c = 8.8$ s that produces $d = 17.6$ s. The estimate of d_c after Ye et al. (2016) is practically identical. As for d, from the regression of Vallée (2013), $d = 23$ s. Earlier regression of $d(M_w)$ after Houston (2001) (based on inversions of Tanioka & Ruff 1997) gives $d \approx 17$ s. As a summary estimate I use 18 s.

For L, the classical regression of Wells & Coppersmith (1994) predicts $L = 49$ km for all variants of unit tensor stacked. Compilation after Blaser *et al.* (2010) gives $L = 46$ km for pooled data. From Leonard's (2010) data analysis one obtains $L = 40$ for dip-slip and $L = 50$ for strike-slip cases, with average of 45 km. As a summary estimate I use 46 km. Combining with θ and d values selected above this results in $v_r = 2.24$ km s^{-1}. Because using of mixture of crustal and subduction data in L estimate, $c_S = 3.8$ km s^{-1} is used to derive m, resulting in $m = 0.59$. As the final point estimate $m = 0.60$ is taken, and the interval estimate is set as [0.45 0.75].

Scaling of second corner frequency and its relation to that of rms front width

It was found in G14, eq. (10), through numerical simulation, that rms front width, w, is approximately proportional to $1/f_{c2}$, where f_{c2} is the second corner frequency of source spectrum. Therefore, one can expect that scaling of w can be deduced from scaling of f_{c2}. Observational data on scaling of f_{c2} were compiled by Gusev (2013) who found them to show certain scatter. For $\chi = \frac{d \log f_{c2}}{d \log f_{c1}}$ from (Atkinson 1993) one can derive $\chi \approx 0.5$ for Eastern North America data. From (Atkinson & Boore 1998) follows $\chi = 0.46$ for Western USA. From left cut-offs of Mexican acceleration spectra of (Aguirre & Irikura 2007). Gusev (2013) derived $\chi = 0.39$. The trends of interbarrier interval 2ρ, a parameter of the barrier source model, can be hypothetically be used to estimate χ, but this is rather uncertain. If one assumes this possible, from Beresnev & Atkinson (2002) one would obtain $\chi = 0.8$ for Western USA data; from Halldorsson & Papageorgiou (2005) this value will be $\chi = 1$. Gusev (2013) concluded that the value $\chi = 0.5$ can serve as a reasonable first approximation. Assuming kinematic similarity of sources $\chi = -3\frac{d \log f_{c2}}{d \log M_0} = -\frac{d \log f_{c2}}{d \log L}$.

Recently Denolle & Shearer (2016), using abundant good-quality teleseismic data found that for dip-slip sources, the log f_{c2} (log M_0) relationship consists of two branches. At lower $M_w \leq 7$–7.5, $\chi \approx 0.6$, whereas at larger M_w, f_{c2} saturates and χ approaches zero. Such a tendency, as well as the difficulty of estimating f_{c2} from regional data at larger magnitudes, may partly explain the mentioned scatter of estimates of χ. The value $\chi = 0.6$ will be chosen as the preferred point estimate, with the assumed range of scatter (0.45–0.75). It corresponds to magnitudes $M_w \leq 7.5$. For larger magnitudes, as one can derive from Denolle & Shearer (2016), ruptures seem to be definitely confined in width; thus, it is hardly adequate to confront their observed trends to the present results of simulation of unbounded propagation of rupture. On the basis of the mentioned simulation results of G14, the estimates of χ will be treated as estimates of λ.